10.1098/rsta.2004.1452

THE ROYAL SOCIETY

Raman spectroscopy of amorphous, nanostructured, diamond-like carbon, and nanodiamond

By Andrea Carlo Ferrari and John Robertson

Department of Engineering, University of Cambridge, Trumpington Street, Cambridge CB2 1PZ, UK (acf26@eng.cam.ac.uk)

Published online 28 September 2004

Raman spectroscopy is a standard characterization technique for any carbon system. Here we review the Raman spectra of amorphous, nanostructured, diamond-like carbon and nanodiamond. We show how to use resonant Raman spectroscopy to determine structure and composition of carbon films with and without nitrogen. The measured spectra change with varying excitation energy. By visible and ultraviolet excitation measurements, the G peak dispersion can be derived and correlated with key parameters, such as density, sp^3 content, elastic constants and chemical composition. We then discuss the assignment of the peaks at 1150 and 1480 cm^{-1} often observed in nanodiamond. We review the resonant Raman, isotope substitution and annealing experiments, which lead to the assignment of these peaks to trans-polyacetylene.

Keywords: Raman spectroscopy; diamond-like carbon; nanodiamond

1. Introduction

Raman spectroscopy is a popular, non-destructive tool for structural characterization of carbon films. The other contributions in this Theme Issue review the application of Raman spectroscopy to graphite, nanotubes, fullerenes, diamond and aromatic molecules. Here we review the model we proposed to explain the trends of the Raman spectra of any amorphous, disordered and diamond-like carbon at any excitation wavelength (Ferrari & Robertson 2000, 2001*b*; Ferrari *et al*. 2003). We show that a bridge between the 'molecular' and 'solid-state' interpretation of the D peak in carbons can be built by considering the electron–phonon coupling matrix elements in graphite (Piscanec *et al*. 2004*a*). We discuss the identification of the non-diamond phases often present in nanodiamond.

2. Classification of carbon films

The great versatility of carbon materials arises from the strong dependence of their physical properties on the ratio of sp^2 (graphite-like) to sp^3 (diamond-like) bonds (Robertson 2002). There are many forms of sp^2 bonded carbons with various degrees

One contribution of 13 to a Theme 'Raman spectroscopy in carbons: from nanotubes to diamond'.

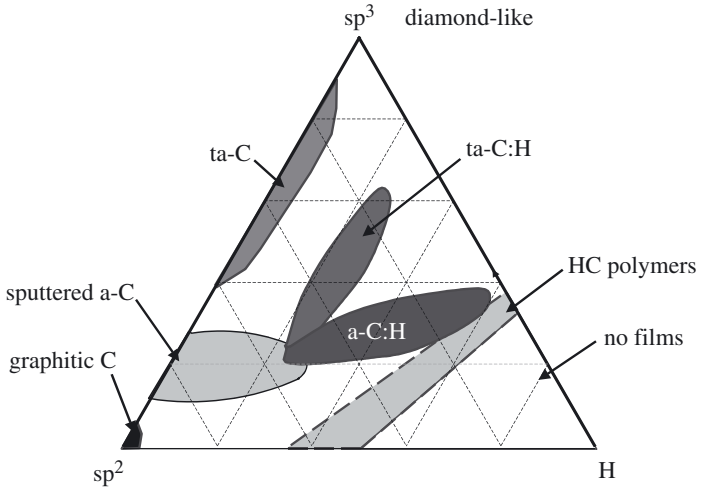

Figure 1. Ternary phase diagram of amorphous carbons. The three corners correspond to diamond, graphite and hydrocarbons, respectively.

of graphitic ordering, ranging from micro-crystalline graphite to glassy carbon. In general, an amorphous carbon can have any mixture of sp^3, sp^2 and even sp^1 sites, with the possible presence of hydrogen and nitrogen. The compositions of nitrogen-free carbon films are conveniently shown on the ternary phase diagram in figure 1.

We define diamond-like carbon (DLC) as an amorphous carbon (a-C) or a-C:H with a significant fraction of sp^3 bonds. It can have a high mechanical hardness, chemical inertness, optical transparency, and it is a wide-band-gap semiconductor (Robertson 2002). DLC films have widespread applications as protective coatings in areas such as optical windows, magnetic storage disks, car parts, biomedical coatings and as micro-electromechanical devices.

a-C:H often has a rather small C–C sp^3 content. DLCs with highest sp^3 content (80–90%) are called tetrahedral amorphous carbon (ta-C) and the hydrogenated analogue ta-C:H. The key parameters of interest in such materials are

(1) the sp^3 content;

(2) the clustering of the sp^2 phase;

(3) the orientation of the sp^2 phase;

(4) the cross-sectional nanostructure;

(5) the H content.

The sp^3 content alone mainly controls the elastic constants, but films with the same sp^3 and H content but different sp^2 clustering, sp^2 orientation or cross-sectional nanostructure can have different optical, electronic and mechanical properties (Robertson 2002). Indeed, the clustering of the sp^2 phase should be added as a fourth dimension in the ternary phase diagram of figure 1, and plays a crucial role in Raman spectroscopy.

Nano-structured sp^2 carbon films are interesting in their own right. They are particularly attractive for electrochemical applications, for supercapacitors, sensors or

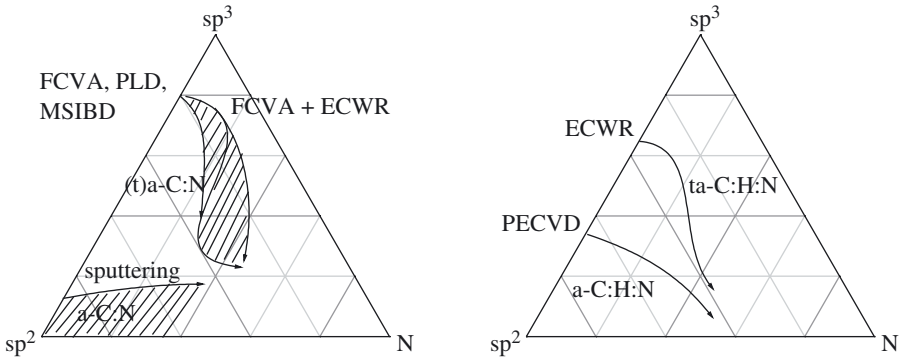

Figure 2. Ternary phase diagrams of amorphous carbon nitride alloys, (*a*) without hydrogen, (*b*) with hydrogen, showing sp^2 C, sp^3 C and N.

fuel cells. Nanostructured carbon films can be produced by cathodic arc or magnetron sputtering in the presence of a relatively high gas pressure to favour the aggregation of sp^2 clusters to be incorporated in the films. Supersonic cluster beam deposition can also be used to grow nanostructured thin films where the original carbon cluster structure is substantially maintained after deposition (Milani *et al*. 1997; Milani & Iannotta 1999). These films are characterized by a memory effect, i.e. they are partially reminiscent of the precursor clusters. Small carbon clusters may have chain or ring structures, whereas larger clusters have the tendency to form three-dimensional cage-like structures characterized by sp^2 coordination. Peculiar to these films is often the presence of carbon sp^1 chains.

Another important class of carbon films is carbon nitrides. Research in these materials was fuelled by the prediction by Liu & Cohen (1989) of a C_3N_4 phase with a bulk modulus and hardness higher than diamond. However, despite massive efforts, there has been no agreed success on the synthesis of crystalline β-C_3N_4 (Badzian *et al*. 1999; Matsumoto *et al*. 1999; Muhl & Mendez 1999). Many of the experiments produced instead amorphous carbon nitrides (a-CN_x), which are of interest in their own right (Badzian *et al*. 1999; Muhl & Mendez 1999). They show promising tribological properties (Cutiongco *et al*. 1996; Hellgren *et al*. 1999). Indeed, amorphous carbon nitrides are presently used as a protective coating for many hard disks and read heads (Cutiongco *et al*. 1996; Casiraghi *et al*. 2004*a*; Ferrari 2004).

It is possible to classify the bonding in carbon nitride films into four types, based on the bonding in the corresponding N-free film as defined in figure 1. The changes in the properties of carbon nitride films as N content is increased should be compared with the properties of the corresponding N-free films. Thus, the variation of mechanical and electronic properties when N is added to an sp^2 bonded carbon film differs from when N is added to a high sp^3 film. This is true whether H is present or not. We classify carbon nitrides into four types: (a) the mainly sp^2 bonded a-C:N produced by sputtering; (b) the mainly sp^3 bonded ta-C:N produced by filtered cathodic vacuum arc (FCVA) pulsed laser deposition (PLD) or mass selected ion beam deposition (MSIBD); (c) plasma deposited a-C:H:N with moderate sp^3 content; and (d) ta-C:H:N prepared by a high-plasma-density source, such as the electron cyclotron wave resonance (ECWR) plasma source, with a higher sp^3 content and lower hydrogen content. The corresponding ternary phase diagrams are shown in figure 2. Note that,

although a general decrease in sp^3 content with N is observed, the precise trends can change for different deposition systems (Ferrari *et al.* 2003). This implies that the sp^3 fraction and the degree of clustering of the sp^2 phase can be different for films of the same N/C ratio (Ferrari *et al.* 2003).

The sputtered a-C:N deserve particular attention. a-C:N films with a high fraction of sp^2 bonded atoms are produced by DC, RF sputtering or magnetron sputtering and by low-energy laser deposition. An unusual aspect of these films is that a-C:N deposited above 200 °C can become nanostructured, with a strong cross-linking between graphitic planes, which gives an increase in mechanical hardness and large elastic recovery (Hellgren *et al.* 1999; Jimenez *et al.* 2000; Gammon *et al.* 2002, 2003). This does not require, however, an increase in the sp^3 fraction (see figure 2*a*), but can rather be seen as an increase in disorder (Jimenez *et al.* 2000; Gammon *et al.* 2002, 2003). Thus N incorporation in this case has an opposite effect to N incorporation in high sp^3 carbons.

Another class of films is the amorphous carbon–silicon alloys (a-C_{1-x}:Si_x:H_y) and hydrogenated carbon–silicon alloys (a-C_{1-x}:Si_x:H_y). They are of interest both in the Si-rich and C-rich composition range (Racine *et al.* 2001). The Si-rich alloys have a wider band gap than a-Si:H and are widely used as p-type window layers in a-Si:H based solar cells (Matsuda & Tanaka 1987). The C-rich alloys are of interest as luminescent materials and as mechanical coating materials. The addition of Si to a-C:H has the beneficial effect of reducing the grown-in compressive stress, improving the thermal stability, and maintaining the low friction coefficient of a-C:H to a higher relative humidity (Oguri & Arai 1992; Gangopadhyay *et al.* 1997). Since Si can only bond sp^3, its incorporation causes the size of the C sp^2 clusters to decrease and opens C sp^2 rings.

There are then many other carbon films studied in literature, such as fluorinated DLCs to be used al low-dielectric-constant insulators for improving the switching performances of circuits (see, for example, Grill 2001), or metal-incorporated films to reduce stress, wear and lower friction (see, for example, Voevodin *et al.* 1996). Here we will not discuss their Raman spectra, since they can be easily understood by considering the effect on the sp^2 clustering of the hetero-atoms and using the rules for the interpretation of the spectra we will present in this review. Clearly, if carbides are formed they will also show their Raman signature.

The last class of carbon films we will consider is the so-called nanocrystalline diamond, also refereed to as nanodiamond or ultra-nanocrystalline diamond. The chemical vapour deposition (CVD) of diamond is an important route in the production of this unique material (Yarbrough & Messier 1990; Angus & Hayman 1998). Generally, the aim is to maximize the crystal quality of CVD diamond. However, diamond grown under non-optimum conditions, such as lower temperature or higher carbon activity in the plasma, gives films with small grain size. Recently, a strong effort is being made to intentionally grow nanodiamond, because smaller grains give films with valuable tribological, mechanical and electrochemical properties (Gruen 1999). The sp^3 phase of this material is crystalline and it is thus very different from ta-C, where the sp^3 phase is amorphous. The remaining sp^2 fraction is a mixture of amorphous carbon and olefinic molecules (Ferrari & Robertson 2001*a*). Here we will consider only the Raman identification of this phase. In another contribution to this issue, Prawer & Nemanich (2004) consider the crystalline sp^3 phase.

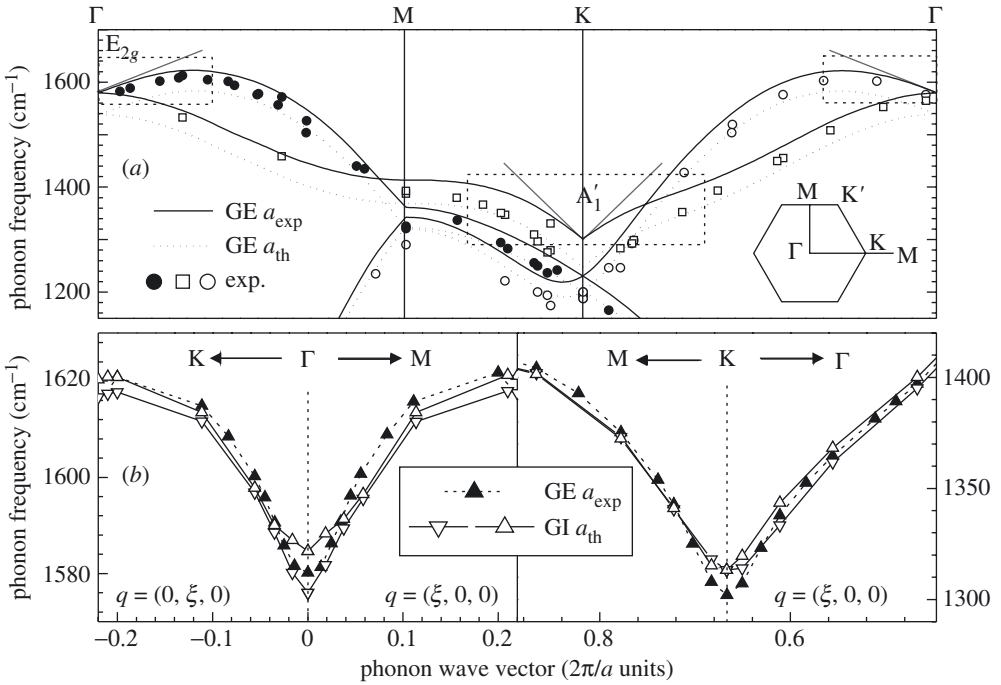

Figure 3. (*a*) Lines are the phonon dispersion of graphene (GE), calculated at the experimental and equilibrium lattice spacings (a_{exp} and a_{th}) from Piscanec *et al.* (2004*a*). Experimental data from Maultzsch *et al.* (2004). The straight lines at Γ and K are obtained from equations (3.1), (3.2). Panels (*b*) correspond to the dotted windows in (*a*). Here, graphite (GI) computed frequencies are also shown. The points are theoretical frequencies obtained by direct calculation. A single graphene band corresponds to two almost-degenerate graphite bands.

3. D and G peak and Kohn anomalies in graphite

Before considering the Raman spectra of carbon films we review some recent results on the much debated issue of the origin of the D peak. This complements the reviews presented in two other contributions to this Theme Issue (Castiglioni *et al.* 2004; Reich & Thomsen 2004). The reader is referred to these two contributions for the description of phonon symmetries, Brillouin zone and band structure of graphite.

The phonon dispersions of graphite have been widely studied through the years and several contrasting theoretical dispersions proposed (Kresse *et al.* 1995; Pavone *et al.* 1996; Mapelli *et al.* 1999; Matthews *et al.* 1999; Gruneis *et al.* 2002; Saito *et al.* 2002; Dubay & Kresse 2003; Maultzsch *et al.* 2004; Wirtz & Rubio 2004). Only recently, the phonon measurements (Maultzsch *et al.* 2004) of the upper optical branches demonstrated, unambiguously, the presence of a large overbending of the A_1' mode at K (Mapelli *et al.* 1999; Maultzsch *et al.* 2004). The phonon dispersion around K is crucial for the correct interpretation of the Raman D peak in defected graphite. This peak is usually attributed to phonon branches around K (Tuinstra & Koening 1970; Pócsik *et al.* 1998; Mapelli *et al.* 1999; Matthews *et al.* 1999; Ferrari & Robertson 2000, 2001*b*; Thomsen & Reich 2000; Gruneis *et al.* 2002; Saito *et al.* 2002; Maultzsch *et al.* 2004) and its dispersion with excitation energy depends on the shape of these branches (Thomsen & Reich 2000).

Piscanec *et al.* (2004*a*) showed that the key point to understanding the D peak is the semi-metallic character of the electronic structure of graphite. In general, the atomic vibrations are partly screened by electronic states. In a metal this screening can change rapidly for vibrations associated to certain $\boldsymbol{q}$ points of the Brillouin zone (BZ), entirely determined by the shape of the Fermi surface. The consequent anomalous behaviour of the phonon dispersion is called Kohn anomaly (Kohn 1959). Kohn anomalies may occur only for wave vectors $\boldsymbol{q}$ such that there are two electronic states $\boldsymbol{k}_1$ and $\boldsymbol{k}_2 = \boldsymbol{k}_1 + \boldsymbol{q}$ both on the Fermi surface (Kohn 1959). The graphite electronic band dispersion is, essentially, described by that of an isolated graphene sheet. In graphene, the gap between occupied and empty electronic states is zero only at the two equivalent BZ points $\boldsymbol{K}$ and $\boldsymbol{K}'$. Since $\boldsymbol{K}' = 2\boldsymbol{K}$, the two equivalent $\boldsymbol{K}$ points are connected by the vector $\boldsymbol{K}$ (see Reich & Thomsen 2004, fig. 6). Thus, Kohn anomalies can occur for $\boldsymbol{q} = \boldsymbol{\Gamma}$ or $\boldsymbol{q} = \boldsymbol{K}$. Piscanec *et al.* (2004*a*) demonstrated that graphite has two significant Kohn anomalies for the $\boldsymbol{\Gamma}$-E_{2g} and $\boldsymbol{K}$-A_1' modes. They also showed that graphite is quite a remarkable case, since a simple analytic description of the Kohn anomalies is possible, unlike all other materials studied so far. The anomalies are revealed by two sharp kinks in the phonon dispersion (figure 3). The slope (α) of these kinks is proportional to the ratio of the square of the electron–phonon coupling (EPC) matrix element and the π bands slope at K ($\beta \approx 14.1$ eV):

$$\alpha_{\Gamma}^{\mathrm{LO}} = \sqrt{3}\pi^2 \frac{\mathrm{EPC}(\Gamma)^2}{\beta} = 397\ \mathrm{cm}^{-1}, \tag{3.1}$$

$$\alpha_{\mathrm{K}} = \sqrt{3}\pi^2 \frac{\mathrm{EPC}(K)^2}{\beta} = 973\ \mathrm{cm}^{-1}. \tag{3.2}$$

And also

$$\frac{\alpha_{\Gamma}^{\mathrm{LO}}\omega_{\Gamma}}{\alpha_{\mathrm{K}}\omega_{\mathrm{K}}} = 2. \tag{3.3}$$

It is thus impossible to derive the phonon branches at Γ and K by force-constant approaches based on a finite number of force constants, as often done in literature (Kresse *et al.* 1995; Pavone *et al.* 1996; Mapelli *et al.* 1999; Matthews *et al.* 1999; Gruneis *et al.* 2002; Saito *et al.* 2002; Dubay & Kresse 2003).

The 'molecular' approach to the origin of the D peak is discussed in the contribution of Castiglioni *et al.* (2004). The 'solid-state' interpretation of the origin of the D peak as due to double resonance (DR) is presented in the contribution of Reich & Thomsen (2004). In general, the 'molecular' and the 'solid-state' interpretations of the D peak do not contradict each other, once the peculiar electron–phonon interaction scenario of graphite is taken into account. Within DR, the D peak Raman intensity is proportional to $\mathrm{EPC}(K)^2$. Graphite has four possible phonons at K, and they should all be Raman active if their EPCs are ignored (Pócsik *et al.* 1998; Matthews *et al.* 1999; Thomsen & Reich 2000; Gruneis *et al.* 2002; Saito *et al.* 2002). But it is a fact that only the D peak has significant intensity (Tuinstra & Koening 1970). In the molecular approach (Mapelli *et al.* 1999; Ferrari & Robertson 2000, 2001*b*), the D peak is assigned to the branch starting from the K-A_1' mode, based on its symmetry and on its large Raman cross-section in aromatic molecules of increasing size. However, this attribution has so far not been universally accepted. In fact, the measured linear D peak dispersion seemed at odds with the flat slope of the highest optical branch near K given by previous calculations (Kresse *et al.*

1995; Pavone *et al*. 1996; Mapelli *et al*. 1999; Dubay & Kresse 2003; Wirtz & Rubio 2004). Because of this, many authors (Pócsik *et al*. 1998; Matthews *et al*. 1999; Thomsen & Reich 2000; Gruneis *et al*. 2002; Saito *et al*. 2002) wrongly assigned the D peak to the doubly degenerate linearly dispersive 1200 cm^{-1} E′ mode at K. The work of Piscanec *et al*. (2004*a*) finally confirmed the attribution of the D peak to the highest optical branch starting from the K-A_1' mode (Tuinstra & Koening 1970; Mapelli *et al*. 1999; Ferrari & Robertson 2000, 2001*b*). Indeed, the A_1' branch has by far the biggest electron–phonon coupling amongst the K phonons. This branch is also linearly dispersive. The Kohn anomaly is the physical origin of this dispersion, which is in quantitative agreement with the measured D peak dispersion (Pócsik *et al*. 1998).

These results have also implications for carbon nanotubes. Due to their reduced dimensionality, metallic tubes display much stronger Kohn anomalies than graphite. This results in phonon softening, implying that folded graphite does not reproduce the phonon dispersions of metallic tubes (Dubay & Kresse 2003; Piscanec *et al*. 2004*b*). The presence of Kohn anomalies in metallic tubes is key in understanding the differences in the Raman spectra between semiconducting and metallic tubes (Piscanec *et al*. 2004*b*).

4. Raman spectra of nitrogen-free carbons

We now review in detail the Raman spectra of carbon films. All carbons show common features in their Raman spectra in the 800–2000 cm^{-1} region: the G and D peaks, which lie at *ca*. 1560 and 1360 cm^{-1}, respectively, for visible excitation, and the T peak at *ca*. 1060 cm^{-1}, seen only in ultraviolet (UV) excitation. The T peak is due to the C–C sp^3 vibrations (Gilkes *et al*. 1997, 2000; Merkulov *et al*. 1997; Ferrari & Robertson 2001*b*). The 'molecular' approach is the simplest way to understand the Raman spectra of amorphous carbons, where no extended graphitic structure exists. It is important to note, nonetheless, that the vibrational and energy levels of clusters can be mapped onto those of graphite. Except for UV excitation, the Raman spectra are dominated by the sp^2 sites, because the excitation resonates with π states. The G and D peaks are due to sp^2 sites. The G peak is due to the bond stretching of all pairs of sp^2 atoms in both rings and chains. The D peak is thus due to the breathing modes of sp^2 atoms in rings. Thus, no rings, no D peak (Tuinstra & Koening 1970; Ferrari & Robertson 2000; Castiglioni *et al*. 2001, 2003, 2004).

We will not consider in detail the second-order spectra of carbon films, since it is usually very small and broad, unless the material is highly graphitic, We will review other first-order features, such as the sp^1 peak at *ca*. 2100 cm^{-1}, sometimes present both in N-free carbons and in carbon nitrides, and the hetero-atoms vibration, which can be detected in UV Raman spectra.

(*a*) *Visible Raman spectra*

The Raman spectra of all carbon films can be described within a three-stage model of increasing disorder (Ferrari & Robertson 2000, 2001*b*), as shown in figure 4. As we move from ordered graphite to nanocrystalline graphite, to amorphous carbon and finally to sp^3 bonded ta-C, the sp^2 groups become first smaller, then topologically

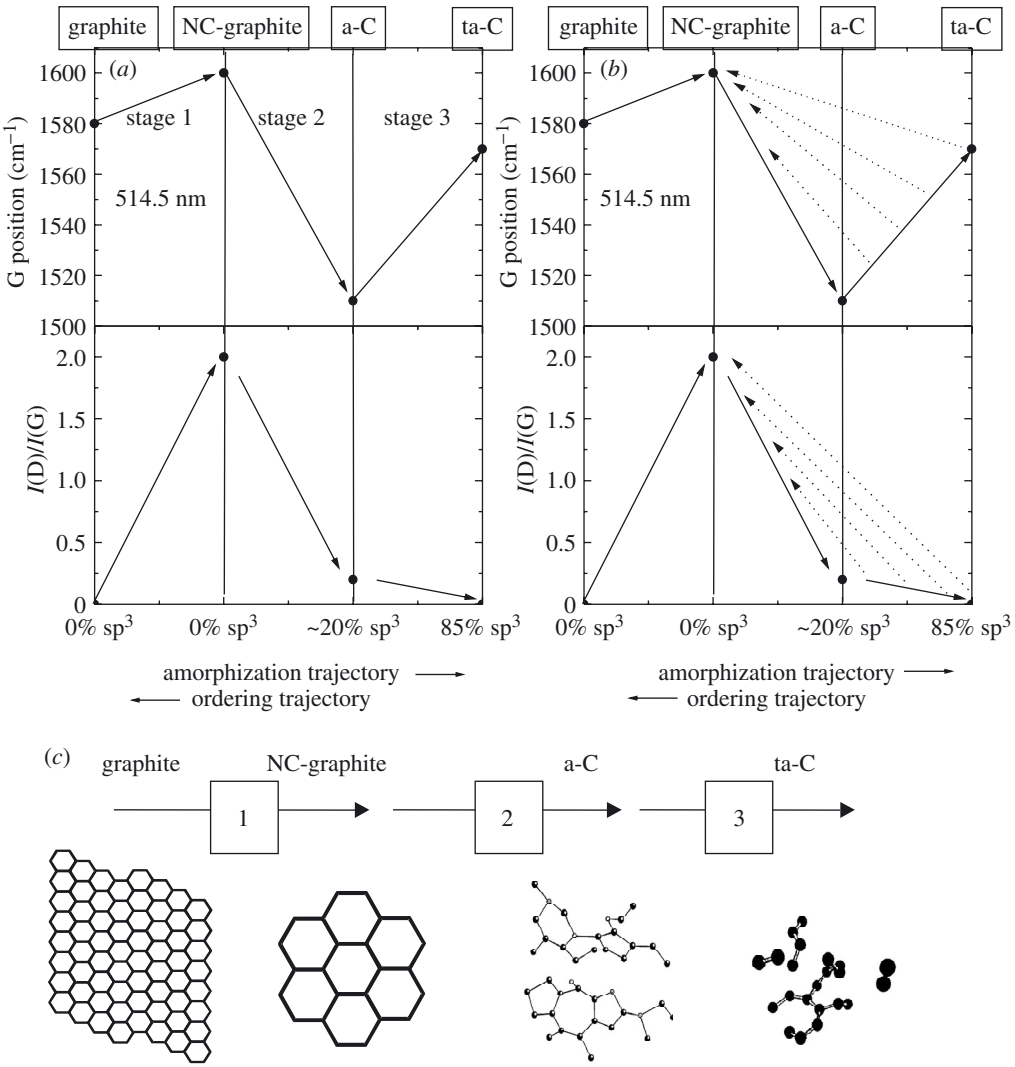

Figure 4. Three-stage model of the variation of the Raman G position and the D-to-G intensity ratio, $I(\mathrm{D})/I(\mathrm{G})$, with increasing disorder (Ferrari & Robertson 2000). The dotted left-pointing arrows in (*b*) mark the non-uniqueness region in the ordering trajectory. (*c*) Variation of the sp^2 configuration in the three amorphization stages.

disordered, and finally change from ring to chain configurations. We call this the *amorphization trajectory*, consisting of three stages from graphite to ta-C, depicted in figure 4*c*:

(1) graphite → nanocrystalline graphite (nc-G),

(2) nanocrystalline graphite → sp^2 a-C,

(3) a-C → ta-C.

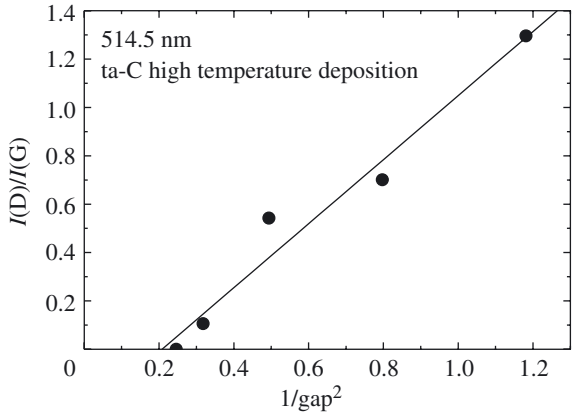

Figure 5. Variation of $I(\mathrm{D})/I(\mathrm{G})$ as a function of $1/(\text{optical gap})^2$ for a series of (t)a-C films deposited with increasing substrate temperature.

The Raman spectra depend on

(i) clustering of the sp^2 phase,

(ii) bond-length and bond-angle disorder,

(iii) presence of sp^2 rings or chains,

(iv) the sp^2/sp^3 ratio.

In visible Raman spectra the cross-section of the sp^2 phase is much higher (50–250 times for 514.5 nm) than that of the sp^3 phase (Wada *et al.* 1980; Salis *et al.* 1996). Furthermore, the spectra depend directly on the configuration of the sp^2 phase and only indirectly on the quantity of the sp^2 phase. Most times the sp^2 configuration varies consistently with the sp^2 fraction. However, in some cases the sp^2 configuration can be changed independently from the sp^2:sp^3 ratio. This phenomenon, which we called hysteresis or non-uniqueness (Ferrari & Robertson 2000), typically happens for high-temperature deposition, annealing after deposition, low-dose ion implantation or unfiltered deposition processes. Figure 4*a* shows the trends in the G and D peaks for the three stages for 514.5 nm excitation.

Broadly, stage 1 corresponds to the reduction of the in-plane correlation length L_a within an ordered graphite layer. The average G peak position moves from 1581 cm^{-1} to *ca.* 1600 cm^{-1}. The D peak appears and increases in intensity following the Tuinstra & Koening (1970, henceforth 'TK') relation, $I(\mathrm{D})/I(\mathrm{G}) \propto 1/L_\mathrm{a}$.

Stage 2 is the introduction of topological disorder into the graphite layer. The bonding is still mainly sp^2, but the weaker bonds soften the vibrational modes, so the G peak decreases to *ca.* 1510 cm^{-1}. The TK relation is no longer valid, but $I(\mathrm{D})/I(\mathrm{G}) \propto L_\mathrm{a}^2$ (Ferrari & Robertson 2000), i.e. is proportional to the number of aromatic rings. As the band gap varies inversely with L_a, this gives a variation of $I(\mathrm{D})/I(\mathrm{G})$ with $1/(\text{optical gap})^2$ (Ferrari & Robertson 2000). An example of this is shown in figure 5.

Stage 3 is the conversion of sp^2 sites to sp^3 sites and the consequent change of sp^2 configuration from rings to chains. The G peak position moves up to *ca.* 1570 cm^{-1}, due to the confinement of π electrons in shorter chains. $I(\mathrm{D})/I(\mathrm{G}) = 0$ due to

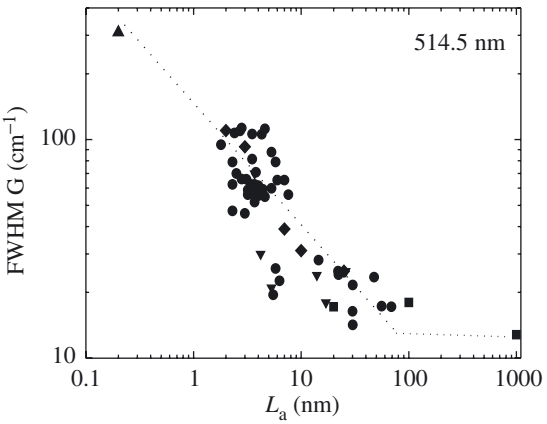

Figure 6. Variation of G peak FWHM with decreasing sp^2 grain size L_a for visible excitation (Ferrari *et al*. 2003). The line is a guide to the eye. The FWHM G-saturates at *ca.* 12 cm^{-1} for high-grain-size graphitic samples.

the absence of rings. Note that figure 5 shows an offset, so that $I(D)/I(G) = 0$ for $1/(\text{optical gap})^2 \neq 0$. This is simply understood if one considers that as-deposited ta-C can have a gap varying between 2.5 and 3.5 eV, but has $I(D)/I(G) \approx 0$, since in ta-C the gap is controlled by the configuration of the sp^2 phase in chains when no rings are present. Thus, we generally expect an offset at around $1/2.5^2$–$1/3.5^2$ eV^{-2} (*ca.* 0.1–0.2 eV^{-2}), which is what observed in figure 5.

On the other hand, the G peak full width at half maximum ($FWHM_G$) is a measure of disorder and increases continuously as the disorder increases (figure 6).

It is possible to derive sp^3 content from the visible Raman spectra *only if there is a relationship between* the sp^2 *and* sp^3 *phases*, for example, between optical gap and sp^3 fraction. To explain this concept, we show how to derive a correlation between visible Raman and sp^3 content for a-C:H films. The main effect of H in a-C:H is to modify its C–C network compared with an a-C of similar sp^3 content. In a-C:H, a higher sp^3 content is achieved mainly by H saturating C=C bonds as CH_x groups, rather than by increasing the fraction of C–C sp^3 bonds (figure 1). Most sp^3 sites are bound to hydrogen (Koidl *et al*. 1990; Ristein *et al*. 1998). Thus, highly sp^3 bonded a-C:H are soft, low density, polymeric films. In a-C:H, the sp^2 sites can exist as rings as well as chains. Increasing H content reduces the sp^2 cluster size and increases the band gap. This gives rise to three bonding regimes. At low H content, sp^2 bonding dominates and the gap is under 1 eV. At intermediate H content, the C–C sp^3 bonding is maximum, the films have the highest density and diamond-like character, and the gap is 1–1.8 eV. At the highest hydrogen contents, the sp^3 content is highest, the bonding is more polymeric and the band gap is over 1.8 eV. Ta-C:H differs in that a higher sp^3 fraction occurs at a fixed lower H content of 25–30% (figure 1). Ta-C:H has much more C–C sp^3 bonding than a-C:H with similar sp^3 fraction, giving a higher density and greater hardness (Morrison *et al*. 1999).

We can derive a relation between visible Raman parameters and sp^3 content for plasma-enhanced chemical-vapour-deposited a-C:H films. From the data compilation of Tamor & Vassel (1994) we can get a general relation between optical gap and 514 nm Raman parameters (figure 7*a*). For as-deposited a-C:H, there is a general relationship between sp^2 content and optical gap, as shown in figure 7*b*. The line in

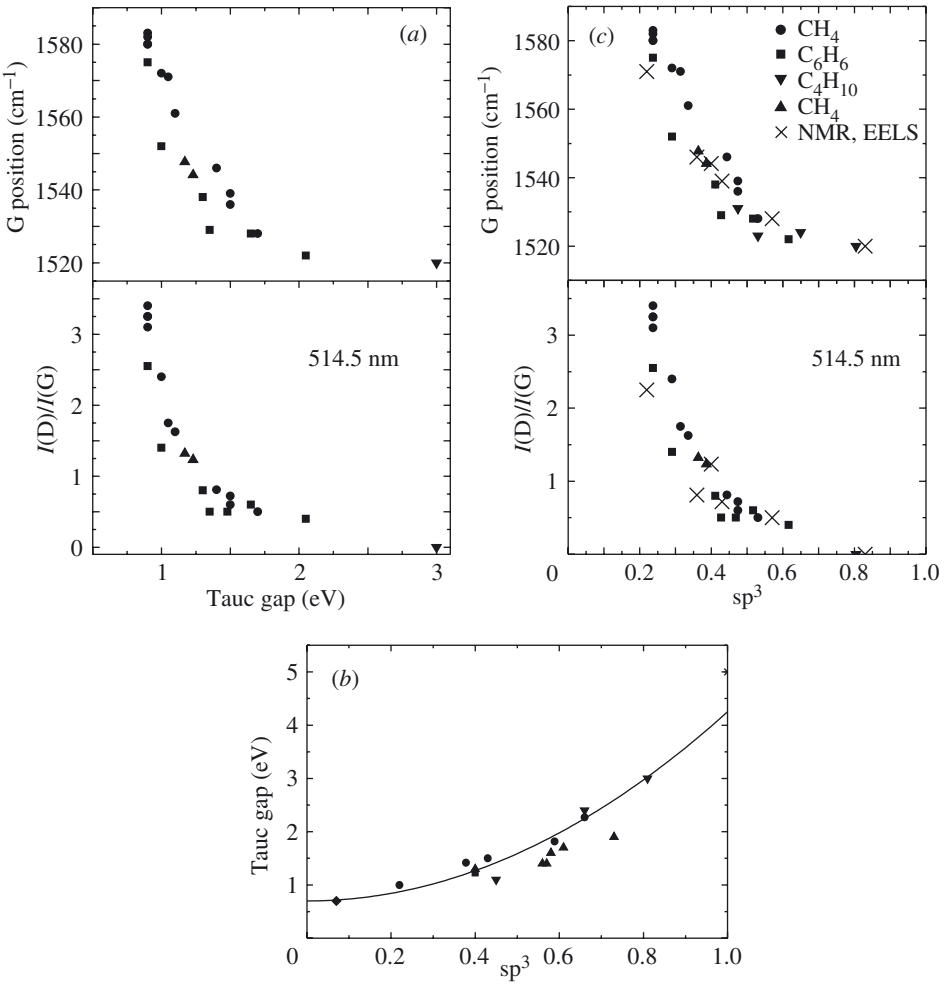

Figure 7. (*a*) G Position and $I(\mathrm{D})/I(\mathrm{G})$ ratio versus optical Tauc gap for as-deposited a-C:H. Data from Tamor & Vassel (1994) and Ferrari & Robertson (2000). The precursor gases are also indicated. Note that a double Gaussian fit was used. (*b*) Optical Tauc gap versus sp^3 content for as-deposited a-C:H. The line is a quadratic fit to the data. (*c*) G Position and $I(\mathrm{D})/I(\mathrm{G})$ ratio versus sp^3 fraction for as-deposited a-C:H. The data are obtained by applying the fit of (*b*) to data in (*a*). Crosses indicate samples for which the sp^3 was measured directly by NMR or EELS.

figure 7*b* is a fit to the experimental data. Applying the fitting line to the data of figure 7*a*, we obtain the relationship between sp^3 content and Raman parameters shown in figure 7*c*. The crosses in figure 7*c* are for samples with sp^3 content directly measured by nuclear magnetic resonance (NMR) or electron energy loss spectroscopy (EELS). They show substantial agreement with the sp^3 content derived by Raman spectroscopy. It is important to note that the relations in figure 7*a*, *c* apply only for 514.5 nm excitation.

In the visible Raman spectra, we can neglect all C–H modes. C–H modes in amorphous carbon films are detectable at much higher photon energy (§ 4). However, a typical signature of hydrogenated samples in visible Raman is the increasing pho-

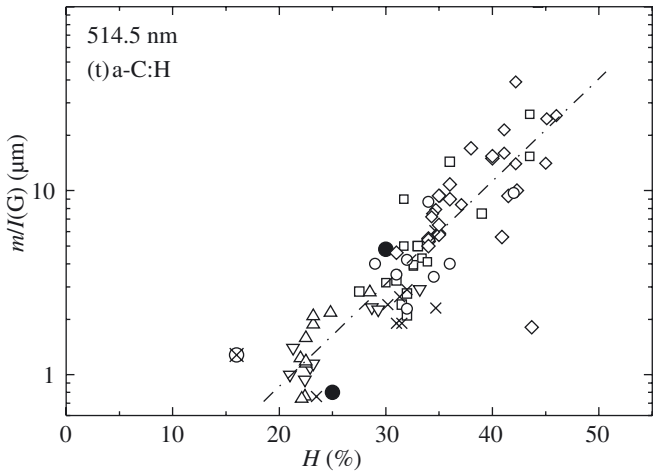

Figure 8. Ratio of the slope, m, of the fitted linear background to the intensity of the G peak, $m/I(\mathrm{G})$ as a function of the bonded H content for a variety of amorphous carbon hydrogenated. (From Casiraghi *et al.* (2004*b*).)

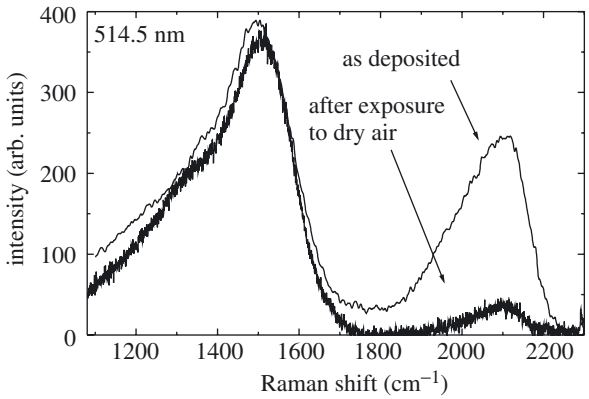

Figure 9. Comparison of visible Raman spectra of an as-deposited cluster-assembled carbon films and the same film after exposure to air. The peak at *ca.* 2100 cm^{-1} is due to linear carbon chains. (From Ravagnan *et al.* (2002).)

toluminescence background for increasing H content. This is due to the hydrogen saturation of non-radiative recombination centres. For H content over *ca.* 40–45%, this background usually overshadows the Raman signal of a-C:H (Marchon *et al.* 1997; Casiraghi *et al.* 2004*b*). The ratio between the slope, m, of the fitted linear background and the intensity of the G peak, $m/I(\mathrm{G})$, can be empirically used as a measure of the bonded H content (Marchon *et al.* 1997; Casiraghi *et al.* 2004*b*), as shown in figure 8. A detailed discussion of the Raman spectra of hydrogenated amorphous carbon samples is reported in Casiraghi *et al.* (2004*b*).

As-deposited H-free cluster-assembled carbon films can have a significant fraction of CC sp^1 chains. These cumulenic chains produce a prominent peak at *ca.* 2100 cm^{-1} in the Raman spectra (figure 9). Exposure to air almost completely destroys the sp^1 phase and significantly decreases the intensity of this peak (figure 9) (see also Ravagnan *et al.* (2002)).

(*b*) *Multi-wavelength Raman spectra*

The three-stage model can be extended to explain spectra taken at different excitation energy. In § 4 *a* we stressed that, for fixed excitation energy, a different sp^2 configuration can result in different Raman spectra. Here we show that, for a fixed sp^2 configuration, by changing excitation energy we get different Raman spectra. The variation of the Raman spectra with photon energy allows us to gain crucial information on the sp^2 configuration. Figure 10 shows as an example the multi-wavelength Raman spectra of ta-C, ta-C:H, a-C and polymeric a-C:H samples (Ferrari & Robertson 2001*b*).

We concentrate on the G peak. The G peak is always present for any carbon at any excitation energy and it is the best defined peak. It is thus essential to derive the maximum information from this peak alone, before analysing the other peaks in detail. The G peak position increases as the excitation wavelength decreases, from infrared (IR) to UV, as shown in figure 11. We define *G peak dispersion*, the rate of change of the G peak position, as a function of the excitation wavelength. Figure 11 shows a linear variation of the G peak with excitation wavelength. Thus, we can empirically define the G peak dispersion as

$$\text{G disp.}\left(\frac{\text{cm}^{-1}}{\text{nm}}\right) = \frac{\text{G pos.}(244\,\text{nm}) - \text{G pos.}(514.5\,\text{nm})}{(514.5 - 244)\,\text{nm}} \tag{4.1}$$

The dispersion increases with disorder. The G peak does not disperse in graphite itself, in nanocrystalline graphite or in glassy carbon. The G peak only disperses in more disordered carbons, where the dispersion is proportional to the degree of disorder. The G peak dispersion separates the materials into two types. In materials with only sp^2 rings, the G peak dispersion saturates at a maximum of *ca.* $1600\,\text{cm}^{-1}$, the G position in nc-graphite. In contrast, in those materials also containing sp^2 chains, particularly ta-C and ta-C:H, the G peak continues to rise past $1600\,\text{cm}^{-1}$ and can reach $1690\,\text{cm}^{-1}$ at 229 nm excitation in ta-C. Thus, ta-C has the largest dispersion.

Figure 12*a* shows the variation of G position against the *amorphization* trajectory, for four typical wavelengths. We pointed out in § 4 *a* that following the reverse, *ordering* trajectory, from ta-C to graphite, there can be non-uniqueness. This means that there can be sp^2 clustering or π electron delocalization without a corresponding $sp^2 \rightarrow sp^3$ conversion. For visible excitation, sp^2 clustering and ordering will always *raise* the G peak in stages 2 and 3 (figure 4*b*). In contrast, in UV excitation, increasing clustering *lowers* the G position. This is shown schematically in figure 12*b*. Comparing visible with UV excitation, there is an *inversion* of the trends. This allows us to discriminate samples, which, although they have different structures, may accidentally show very similar Raman spectra at a certain wavelength, as shown by the various crossing lines in figure 11. Indeed, if the G peak positions of two carbon samples are similar at 514.5 nm but differ in the UV, then the sp^2 clustering is higher for the sample with the lower G peak dispersion (Ferrari & Robertson 2001*b*). Thus, for *any* set of carbon samples, a lower G peak dispersion *always* means ordering and, vice versa, an increase in G peak dispersion *always* means disordering. The G peak dispersion is thus a simple, direct way to characterize amorphous carbons in terms of gap, sp^2 or sp^3 content, or hardness and density.

Figure 13 shows three significant examples of the use and meaning of the G peak dispersion. Figure 13*a* plots the dispersion of the G peak for ta-C:H samples annealed

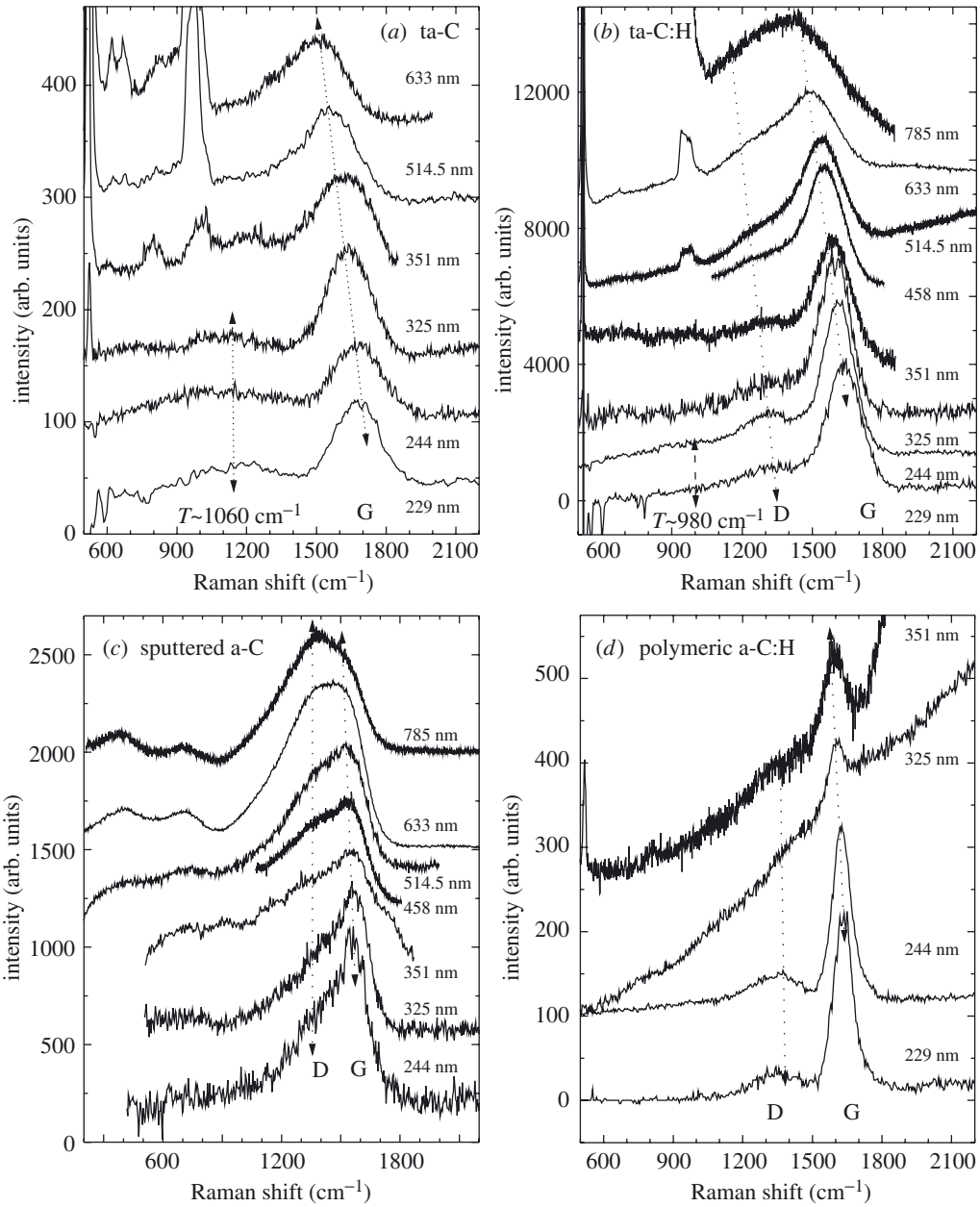

Figure 10. Multi-wavelength Raman spectra of (*a*) ta-C, (*b*) ta-C:H, (*c*) sputtered a-C and (*d*) polymeric a-C:H. The peaks' trends and labels are indicated.

at increasing temperatures. The drop of the G peak dispersion corresponds to the onset of the clustering of the sp^2 phase, just before the onset of sp^3 to sp^2 conversion and H effusion (Conway *et al*. 2000; Ilie *et al*. 2000). Figure 13*b* plots the G peak dispersion as a function of Young's modulus for ta-C films of increasing thickness (Casiraghi *et al*. 2004*a*). A linear relation is found, as expected from the

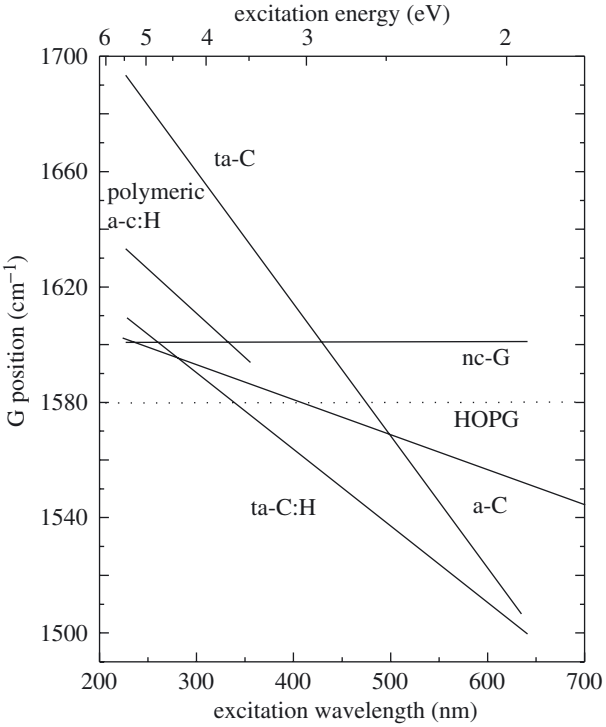

Figure 11. Dispersion of G peak position with excitation wavelength and excitation energy, for highly oriented pyrolytic graphite (HOPG), nc-G, ta-C, ta-C:H, sp^2 a-C and polymeric a-C:H.

above discussion. A final interesting example is shown in figure 13*c*. This plots the G peak position and dispersion as a function of the Si/(Si + C) ratio for a series of (t)a-$C_{1-x}Si_x$:H_y alloys (Racine *et al*. 2001). In this case, for both green and UV excitations, the G peak linearly downshifts with the Si/(Si + C) ratio, thus the dispersion of the G peak is constant with the Si/(Si + C) ratio. This is expected, since an increase in the Si content does not induce further clustering of the sp^2 phase. Si can only be sp^3 bonded and behaves differently from N, giving no hysteresis. Thus, in this case, the Si content can be derived directly from the G position in either green or UV Raman spectra (Racine *et al*. 2001).

A multi-wavelength investigation also provides the $FWHM_G$ for every excitation energy. This is quite useful, since $FWHM_G$ always decreases with increasing disorder, for *every* excitation wavelength and for *every* type of carbon (Ferrari & Robertson 2001*b*; Ferrari *et al*. 2003). The absolute value of $FWHM_G$ decreases with increasing excitation energy and decreases more for more disordered films (Ferrari & Robertson 2001*b*). The $FWHM_G$ does not present non-uniqueness problems so, in principle, it can monitor the carbon bonding even for a single excitation wavelength. In practice, however, it is always advisable to perform a multi-wavelength excitation study, and consider both the G peak dispersion and $FWHM_G$ trends. Is important to have a self-consistency check of the measurements, for at least two different wavelengths, such as 514.5 nm and 244 nm, in order to get more reliable data. As an example, figure 14 shows that the mechanical properties of hydrogenated amorphous carbons can be

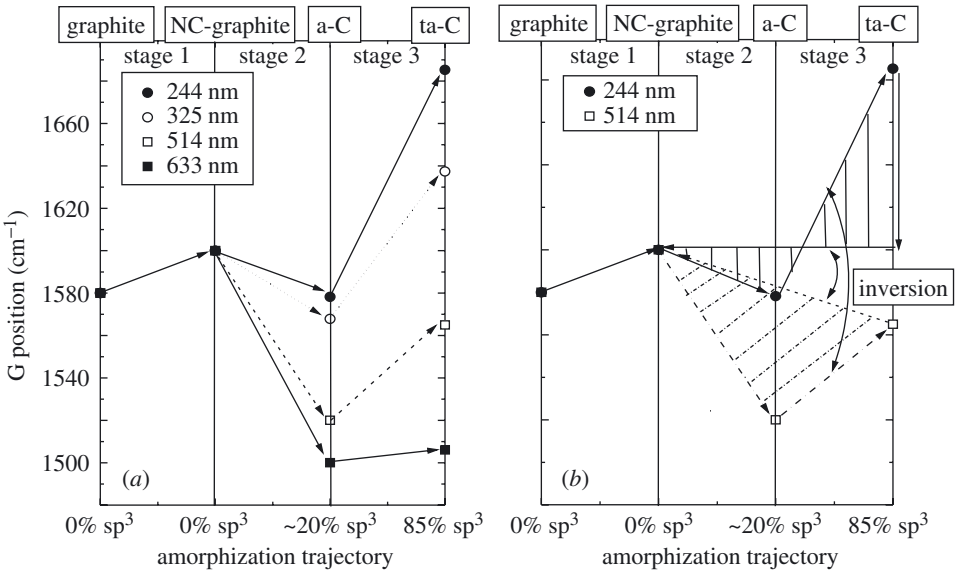

Figure 12. (*a*) Amorphization trajectory, showing the schematic variation of G peak position for four typical wavelengths. (*b*) Amorphization trajectory, showing the possibility of non-uniqueness in stages 2 and 3 for two typical wavelengths (514.5 and 244 nm). The non-uniqueness regions at 514.5 nm and 244 nm are evidenced by lines. Note the trend inversion, with the highest shift vis $\rightarrow$ UV for samples having the least ordered sp^2 phase.

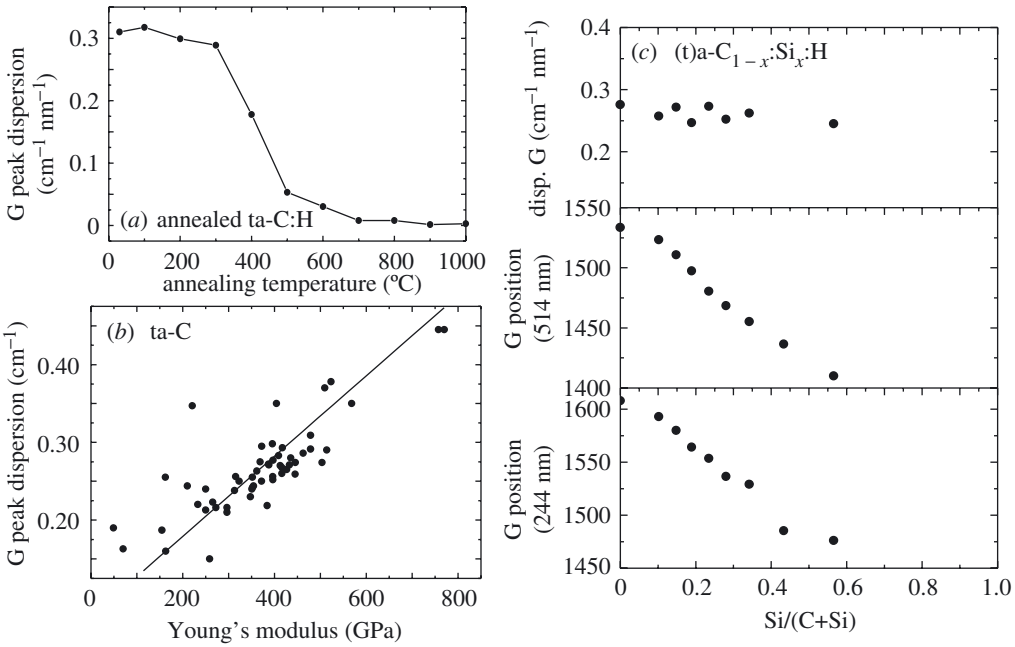

Figure 13. (*a*) G peak dispersion for annealed ta-C:H samples. (*b*) G peak dispersion as a function of the Young modulus for ta-C films. (*c*) Variation of G peak dispersion, 514.5 nm G position and 244 nm G position for a series of (t)a-C_{1-x}:Si_x:H alloys as a function of Si/(C + Si).

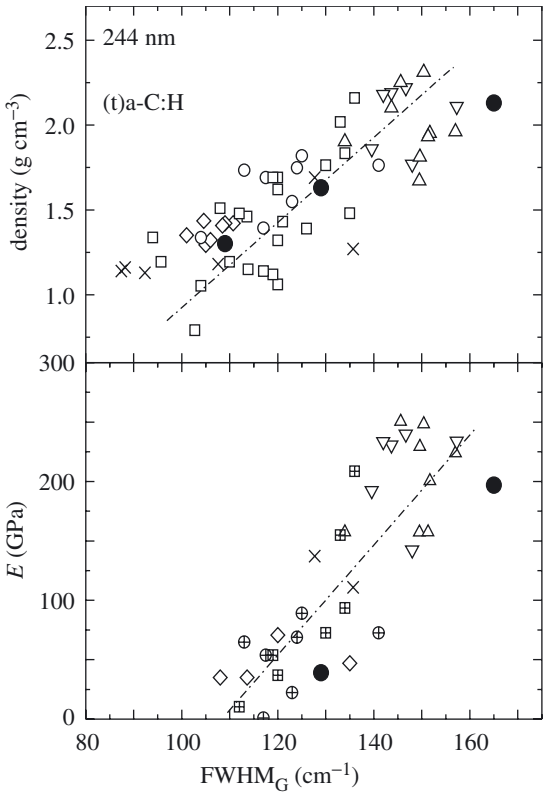

Figure 14. Density and Young's modulus as a function of $\mathrm{FWHM_G}$ measured at 244 nm for a variety of hydrogenated amorphous carbons. (From Casiraghi *et al.* (2004*b*).)

described simply by the $\mathrm{FWHM_G}$ measured at 244 nm, where no photoluminescence is present and clear Raman spectra can be measured (Casiraghi *et al.* 2004*b*).

(*c*) *The T peak and sp*^{3} *content*

The first UV Raman studies (Gilkes *et al.* 1997; Merkulov *et al.* 1997) found a new peak at *ca.* 1060 cm^{-1}, conventionally labelled 'T'. This corresponds to the peak in the CC sp^3 vibration density of states (VDOS) of ta-C in simulations (Kohler *et al.* 1995; Drabold *et al.* 1994) and EELS data (Lopinski *et al.* 1996). Figure 15 gives some empirical relations between the $I(\mathrm{T})/I(\mathrm{G})$ ratio, the T peak position and the sp^3 content (Gilkes *et al.* 2000; Ferrari & Robertson 2001*a*).

The variation of $I(\mathrm{T})/I(\mathrm{G})$ with the sp^3 content is quite nonlinear for 60–90% sp^3 content (figure 15*a*). This can be explained as follows. The UV Raman spectra always possess a large G peak (figure 10). If this is subtracted, this leaves the T peak. As the sp^3 content falls, the VDOS peak at 1060 cm^{-1} shifts upwards to that of an sp^2 network at 1400 cm^{-1} (Lopinski *et al.* 1996). Alternatively, the changes could be represented as a reduction of the T peak at 1060 cm^{-1} and the rise of a peak at *ca.* 1400 cm^{-1}: a D-like peak. Thus, as the sp^2 content of ta-C rises, the T peak intensity (corresponding to the CC sp^3 VDOS) is reduced, with a corresponding increase in a D peak. A complication is that the D peak intensity depends not

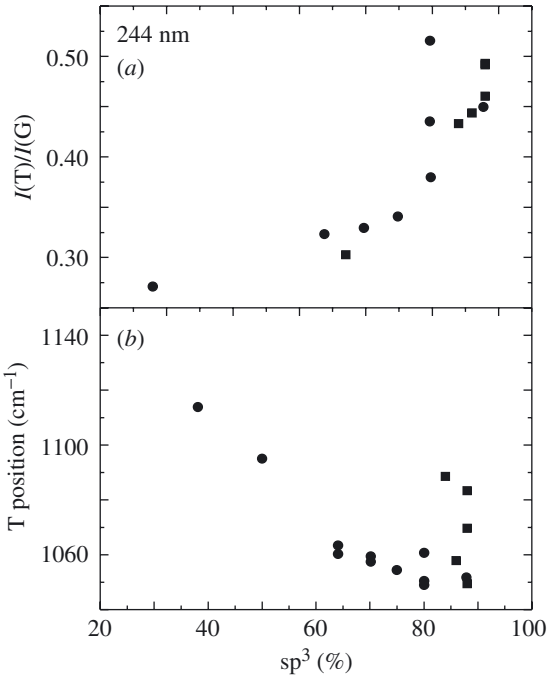

Figure 15. (*a*) $I(\mathrm{T})/I(\mathrm{G})$ and (*b*) T peak position versus sp^3 fraction for non-hydrogenated carbon films.

only on the sp^2 fraction, but also on its order. If the sp^2 sites have graphitic order, the D peak is absent in UV; if the sp^2 sites are in chains, the D peak is absent. Only if the sp^2 sites are in disordered rings does a residual D peak survive in UV (Ferrari & Robertson 2001*b*). This renders the T peak much less useful as a practical characterization tool than originally thought (Gilkes *et al*. 1997; Merkulov *et al*. 1997), especially if compared with the G peak dispersion. However, we can give some qualitative rules on its use.

A T peak at *ca.* $1060\,\mathrm{cm}^{-1}$ and an $I(\mathrm{T})/I(\mathrm{G})$ ratio of about 0.4–0.42 in H-free samples is a sufficient condition to estimate an sp^3 content of *ca.* 80%. An $I(\mathrm{T})/I(\mathrm{G})$ ratio of 0.3–0.4 still indicates an sp^3 content of 60–80%, but sp^2 clustering makes it difficult to give a precise figure. Finally, $I(\mathrm{T})/I(\mathrm{G}) < 0.2$ indicates an sp^3 content lower than 20–30%. Thus the presence of a T peak provides yet another means of resolving non-uniqueness. Indeed, a sample with high sp^3 fraction and high clustering of the sp^2 phase will always show a T peak, even if it is smaller than that of a similar sp^3 content sample, but with limited clustering of the sp^2 phase. On the other hand, a sample with a low sp^3 fraction, but with a similar sp^2 phase clustering and, thus, similar $I(\mathrm{D})/I(\mathrm{G})$ in visible excitation, will not show any T peak. This empirical use of the T peak extends to hydrogenated samples. Figure 10*b* shows that the T peak in ta-C:H or a-C:H is at *ca.* $980\,\mathrm{cm}^{-1}$, lower than in ta-C. This is consistent with the simulations of the C–C sp^3 VDOS in ta-C:H (Mauri & Del Corso 1999). The presence of the residual D peak must be taken into account when fitting. For hydrogenated samples, EELS gives the total fraction of sp^3 bonded C atoms, both as C–C and C–H sp^3 bonds, but the T peak is sensitive only to C–C sp^3 bonds. Indeed, comparing the UV Raman spectra of ta-C:H and polymeric a-C:H (figure 10*b*, *d*), it is clear that

most C sp^3 atoms are bonded to H in polymeric a-C:H, due to the absence of a clear T peak, while in ta-C:H there is a sizeable number of C–C sp^3 bonds. Empirically, $I(\mathrm{T})/I(\mathrm{G}) \approx 0.1$–$0.2$ in (t)a-C:H indicates an overall sp^3 content of *ca.* 70%. Again, as sp^2 clustering also contributes to a D peak, this can make things more difficult.

(*d*) Ab initio *calculations of resonant Raman spectra*

Calculations of Resonant Raman spectra of model ta-C structures have recently become feasible (Profeta & Mauri 2001; Piscanec *et al.* 2004*c*). This is a major improvement, since the previous approaches based on the vibrational density of states were not appropriate to explain any resonant phenomenon. Piscanec *et al.* (2004*c*) calculated the Raman spectra of a variety of different amorphous carbon random networks with varying sp^3 content, density and local sp^2 arrangement. The resonant Raman intensities were evaluated by a tight-binding method, which extends Placzek's approximation of the non-resonant Raman intensities to include resonance (Profeta & Mauri 2001).

Figure 16 shows an excellent agreement between the simulated Raman spectra of a model ta-C sample for excitation wavelengths varying from 633 to 233 nm and the measured spectra in a real ta-C. The double structure of the G peak in the calculated spectra is an artefact due to the small number of sp^2 sites, organized as dimers and short chains (up to six atoms), in the 64-atom model (figure 17).

Figure 16*a* also shows the relative contributions of vibrations coming from sp^2 and sp^3 atoms. It confirms that the T peak is really due to C–C sp^3 vibrations and that it only appears for UV excitation, while its contribution is negligible for visible excitation. It is also verified that, for *ca.* 5 eV excitation, the sp^2 and sp^3 cross-sections are roughly the same (Profeta & Mauri 2001), in agreement with the assumption that 244 nm Raman gives an evenly weighted probe of the sp^2 and sp^3 phases (Ferrari & Robertson 2001*b*). Only for energies higher than 6 eV would the sp^3 C atoms provide 90% of the total intensity. It would thus be of interest to explore such a high-excitation-energy region.

Figure 18 shows that the calculated G peak positions as a function of the excitation energy are consistent with the experimental ones (Piscanec *et al.* 2004*c*).

5. Raman spectra of carbon nitrides

We now consider the effect of nitrogen on the Raman spectra. (For a review of the IR spectra of carbon nitrides see Ferrari *et al.* (2003).) The vibration frequencies of solid carbon nitrides are expected to lie close to the modes of the analogous unsaturated CN molecules, which are 1500–1600 cm^{-1} for chain-like molecules and 1300–1600 cm^{-1} for ring-like molecules (Dollish *et al.* 1974; Katkritzki 1963, 1971). This means that there is little distinction in the G–D region between modes due to C or N atoms. For example, the frequency of bond-stretching skeletal and ring modes is very similar in benzene, pyridine and pyrrole, so it is difficult to assess if an aromatic ring contains nitrogen or not. The modes in amorphous carbon nitrides are also delocalized over both carbon and nitrogen sites because of the nitrogen tendency to sp^2 clustering. There is therefore little difference between the Raman spectra of carbon nitrides and N-free carbon films in the 1000–2000 cm^{-1} region.

The similar frequencies of C–C and C–N modes could make the interpretation of the skeletal modes quite difficult, if one is hoping to single out C–N and N–N modes,

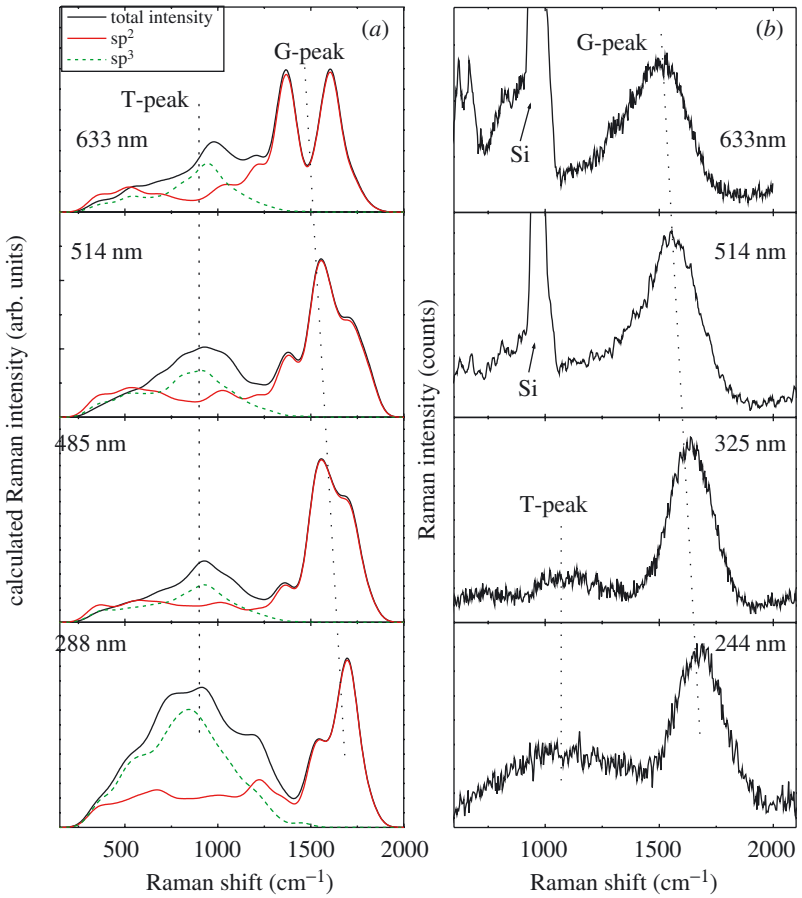

Figure 16. (*a*) Calculated Raman spectra for a set of different excitation wavelengths for the model ta-C sample shown in figure 17. (From Piscanec *et al.* (2004*c*).) The total Raman spectra are decomposed in the contributions from sp^2 and sp^3 atoms. The double peak structure of the G peak is an artefact due to the small number of sp^2 sites in the model ta-C. (*b*) Measured Raman spectra.

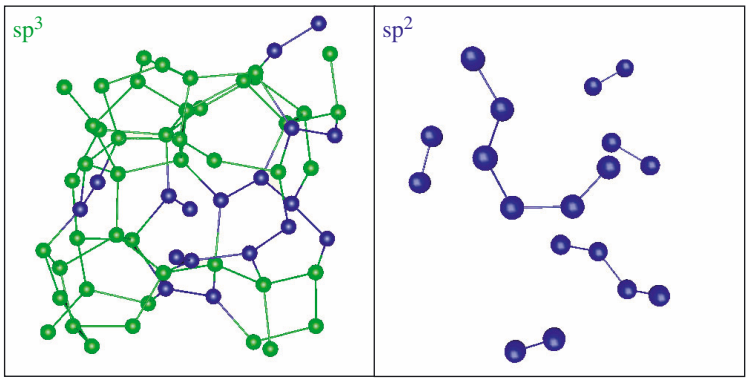

Figure 17. Sixty-four-atom model ta-C used for the calculations in figure 16.

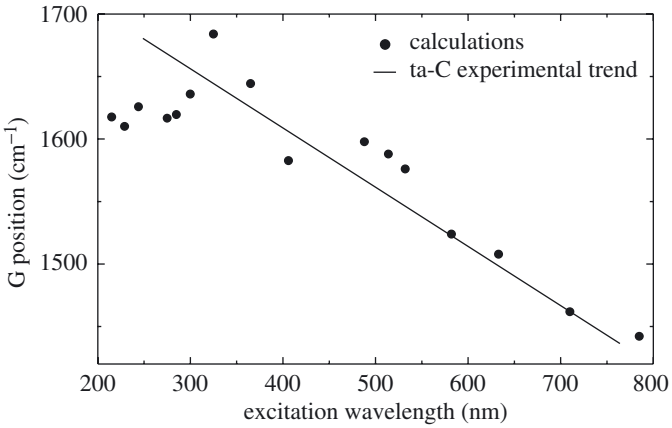

Figure 18. Comparison of the calculated G peak positions as a function of excitation wavelength and experimental ones. (From Piscanec *et al.* (2004*c*).)

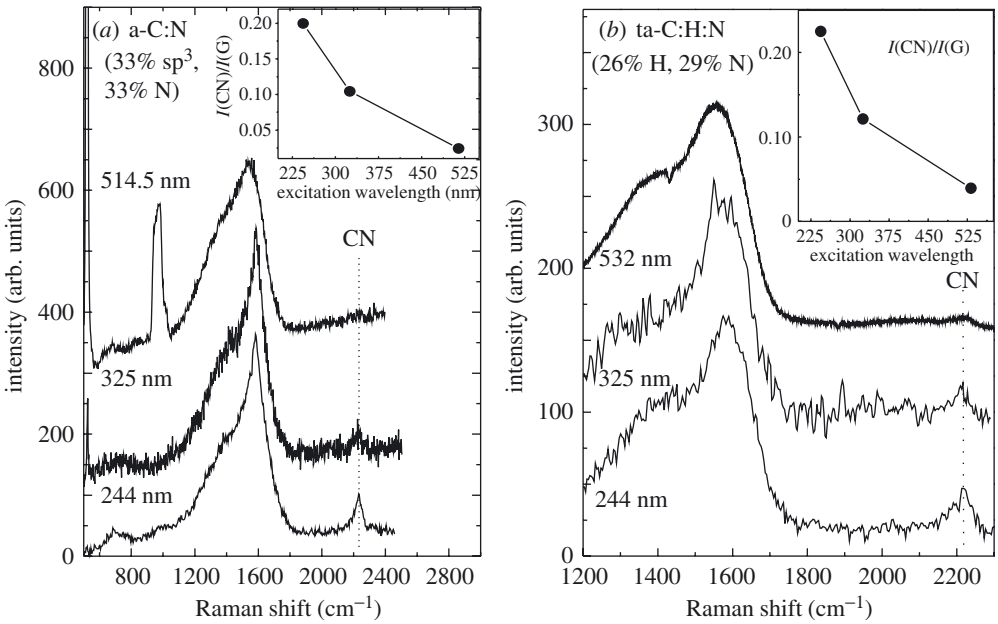

Figure 19. (*a*) Multi-wavelength Raman spectra of a 33% sp^3, 33% N a-C:N. For 514.5 nm and, to a lesser extent, 325 nm excitations, the contributions of the substrate Si Raman peaks at *ca.* 521 and 970 cm^{-1} are also seen. (*b*) Multi-wavelength Raman spectra of a ta-C:H:N film with *ca.* 26% H and 29% N. The insets show the increase in the relative intensity of the CN sp peak, $I(\mathrm{CN})/I(\mathrm{G})$, with decreasing excitation wavelength.

as was often done in previous works (Wixom 1990; Chowdhury *et al.* 1998; Fung *et al.* 1999; Yap *et al.* 1998). However, there is no proof that the direct contribution of these modes in the 1000–2000 cm^{-1} region can be detected (Ferrari *et al.* 2003). Instead, we analyse the trends in the G and D positions in the same way as in the N-free samples. This enables us to explain in a simple way the observed spectra in the 1000–2000 cm^{-1} region, without the need to invoke specific contributions of

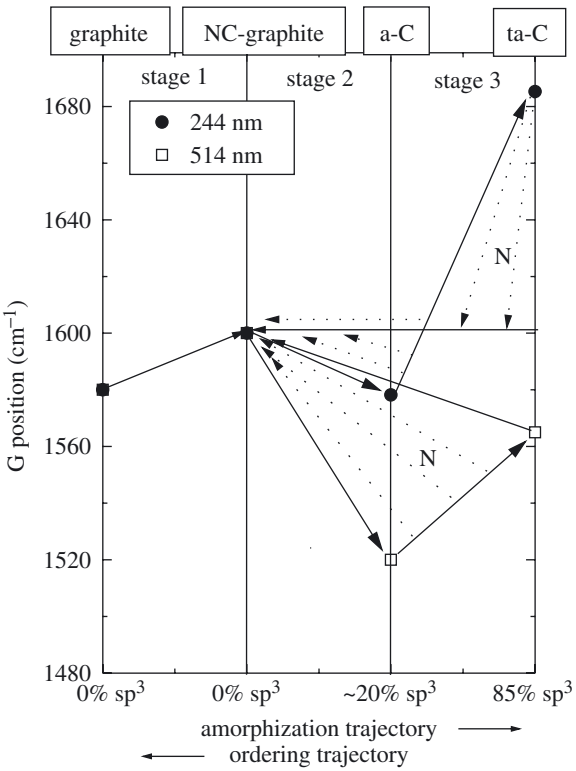

Figure 20. Three-stage model of the variation of the G peak position versus disorder for visible and UV excitation in amorphous carbon nitrides. The bold right-pointing arrows represent the amorphization trajectory in stages 2 and 3. The 'bow-tie' and triangular-shaped regions defined by the dotted and continuous left-pointing arrows indicate the non-uniqueness regions for UV and visible excitations respectively. N introduction generally induces non-uniqueness in stage 3, as indicated by the letter 'N' in the graph.

heteropolar modes. Figure 19 shows as an example the Raman spectra of a cathodic-arc-deposited (t)a-C:N (type (b) in the classification of § 2) and a (t)a-C:H:N film of type (d).

The three-stage model can be simply extended to explain the trends in the Raman parameters in any carbon nitride measured at any excitation wavelength. In particular, we consider the trends in the G peak position.

Figure 12*b* can be modified easily to explain carbon nitrides by recalling that, in general, adding N causes an independent evolution of the sp^3 fraction and sp^2 clustering. This causes a non-uniqueness of the sp^2 configuration for a given sp^3 content. This means that the ordering trajectory induced by adding N to ta-C or ta-C:H is not equivalent to the reverse of the amorphization trajectory leading from a-C to ta-C. Thus, for a certain sp^3 content, we can have various G peak positions, in both visible and UV excitation. This effect is summarized for N-free carbons in figure 12*b*, by the regions defined by the dotted arrows pointing in the ordering direction. These indicate the various G peak positions that could correspond to a given sp^3 content. Figure 12*b* can be simply updated to predict the trends of G peak position in carbon nitrides, as shown in figure 20. This plots the schematic variation

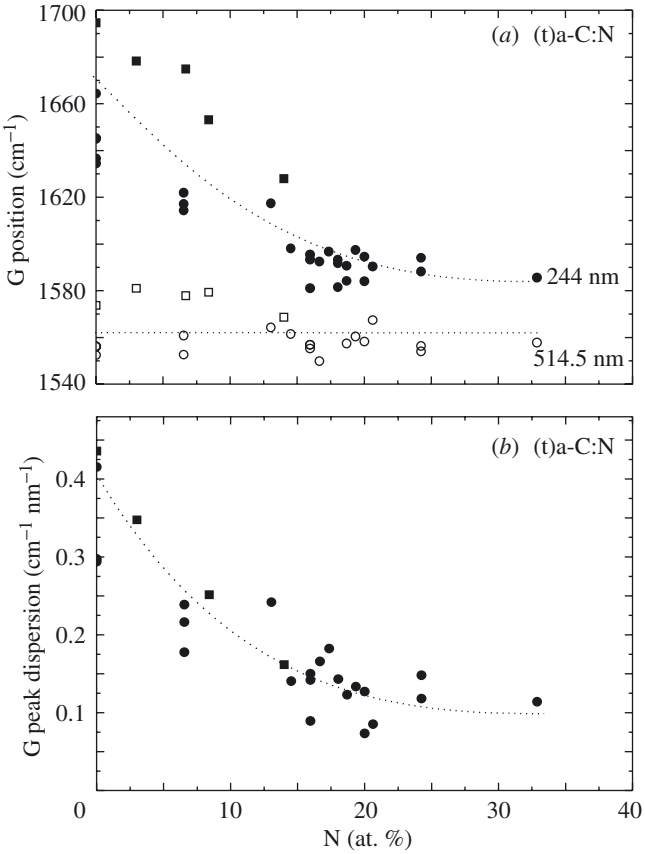

Figure 21. (*a*) G peak position versus N content for 244 and 514 nm excitation for (t)a-C:N films. (*b*) Dispersion of G peak versus N content. The lines are guides to the eye.

of G peak position for 244 nm and 514 nm excitations in carbon nitrides. Figure 20 is the same as figure 12*b*, except that now we consider the non-uniqueness regions as triggered by N introduction in high sp^3 samples (as further stressed by the letter N used in figure 20 to define these regions).

Figures 21–23 plot the trends in G peak position and dispersion for (t)a-C:N, (t)a-C:H:N and high substrate temperature sputtered a-C:N films. Figure 20 immediately allows us to understand the trends of figures 21–23. Clustering in UV Raman causes a G peak downshift with increasing N content for stage 3 carbons. Clustering is synonymous with the ordering trajectory in figure 20. The possible downshift is larger for higher initial G peak positions above 1600 cm^{-1}. In contrast, clustering increases the G peak position for visible excitation—the lower the initial G peak position, the larger this upshift is. Thus, following the ordering trajectory, the G peak trends for UV and visible excitation are *opposite* for stage 3 carbons. This is seen in figures 21*a* and 22*a*. Furthermore, the *trend inversion*, between visible and UV Raman, causes a higher G peak dispersion for lower sp^2 clustering, i.e. for lower N content in carbon nitrides. This is seen experimentally in figures 21*b* and 22*b*. The G peak dispersion again proves to be a crucial parameter in resolving the ambiguity that non-uniqueness can cause for single-excitation-energy measurements.

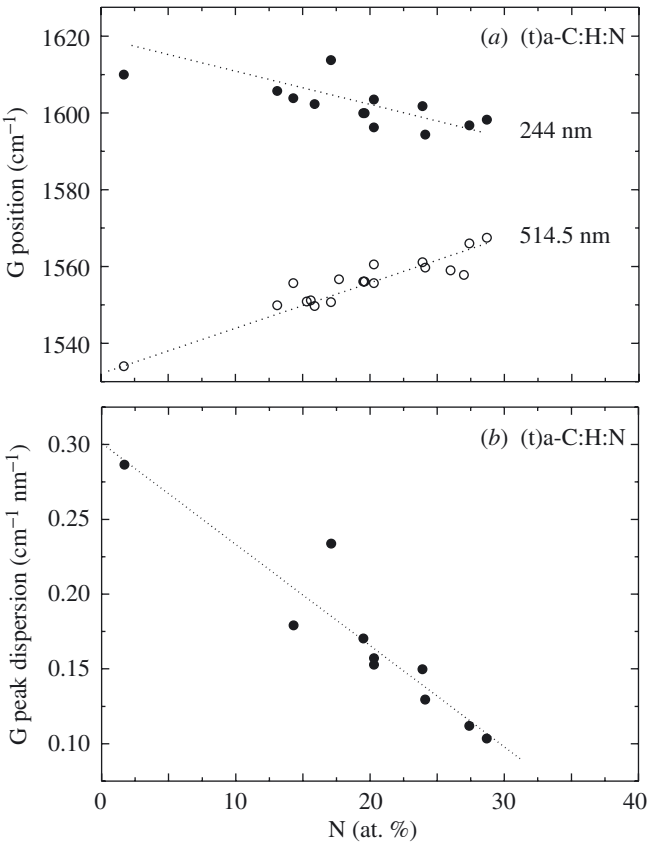

Figure 22. (*a*) Variation of G peak position with N content at 244 and 514 nm excitation for (t)a-C:H:N films. (*b*) variation of G peak dispersion with N content. The lines are guides to the eye.

In § 2 we stressed that N addition in a-C may increase its hardness and elastic recovery, especially at temperatures higher than 200 °C. In this case, N does not cause more clustering of sp^2 sites, but does cause more cross-linking and thus increases disorder, even though this is not necessarily through an sp^3 increase (Jimenez *et al.* 2000; Gammon *et al.* 2002, 2003). These a-C:N can thus be classified as stage 2 carbons with increasing amorphization. From figure 20, we see that the amorphization trajectory for stage 2 carbons gives a decrease in G peak position for both visible and UV Raman spectra (bold right-pointing arrows). Figure 20 also predicts a larger decrease for 514 nm excitation. This implies that the G peak dispersion must increase for increasing N content. This is precisely what is seen experimentally in figure 23*a*, *b*.

In general, N can also increase sp^2 clustering even for stage 2 carbons, e.g. for samples deposited at room temperature. In this case, figure 20 predicts a rise of G position in the visible and *also* in UV excitation (dotted left-pointing arrows), but without the trend inversion typical of stage 3 carbons. However, the increase in G position with N for UV excitation is lower than the corresponding upshift for visible excitation. Thus, even without trend inversion, this again results in a lower G peak dispersion with increasing N content. Thus, as for *any* carbon, also for carbon

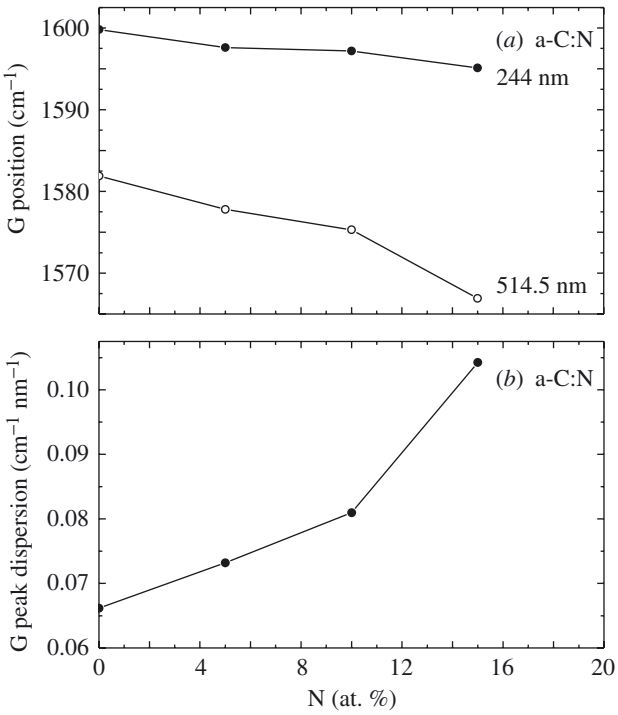

Figure 23. (*a*) Variation of G peak position with N content for 244 and 514 nm excitation for high-temperature-deposited sputtered a-C:N films. (*b*) Variation of G peak dispersion with N content.

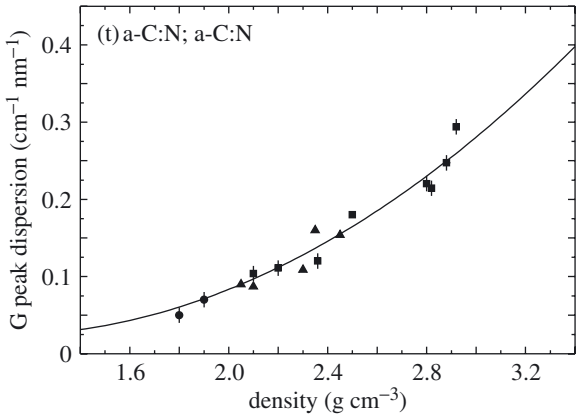

Figure 24. G peak dispersion as function of the mass density for different carbon nitride films deposited by cathodic arc and sputtering. A clear correlation over a large density region is seen.

nitrides a lower G peak dispersion *always* means ordering and, vice versa, an increase in G peak dispersion *always* means disordering. A clear example of this is plotted in figure 24, where a wide collection of G peak dispersions and density data on various carbon nitrides produces an unambiguous relation.

In a similar way, we can easily extend to carbon nitrides the interpretation of the T peak as due to C–C sp^3 vibrations. An example of this is shown in figure 25,

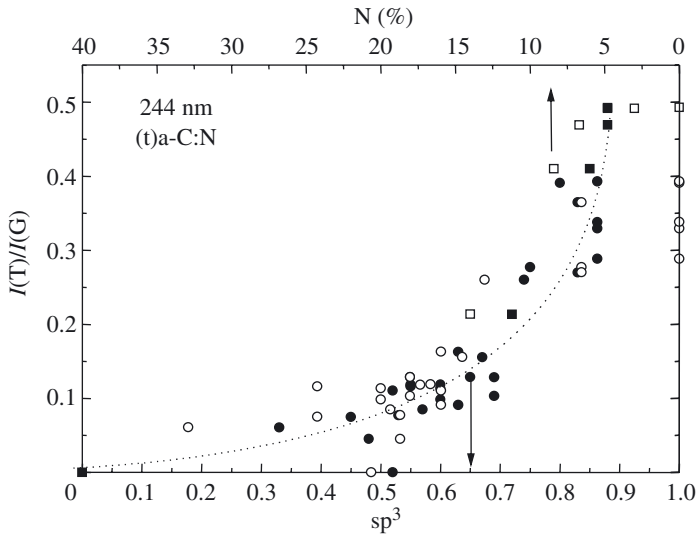

Figure 25. Variation of $I(\mathrm{T})/I(\mathrm{G})$ with sp^3 content (lower scale, solid symbols) and N content (upper scale, open symbols) for (t)a-C:N films. The lines are guides to the eye.

where the $I(\mathrm{T})/I(\mathrm{G})$ ratio is plotted as a function of sp^3 content and N content for a series of (t)a-C:N films. It is interesting to note that the trends in both the upper and lower axes are very similar. This again shows that N introduction in high sp^3 carbons induces an increase in the sp^2 phase clustering and decrease in the sp^3 content.

6. Detection of hetero-atoms by UV Raman spectroscopy

In § 4 *c* we pointed out that UV Raman spectra can detect the C–C σ bonds, due to the increase in their cross-section with respect to the π bonds. This is more general, in that any σ bonds between hetero-atoms can be seen for UV excitation. This implies that UV Raman spectroscopy can be a useful complementary tool to IR spectroscopy for elemental detection.

Figure 10*d* plotted the multi-wavelength Raman spectra of polymeric a-C:H. Figure 10*d* shows that for decreasing excitation energy the photoluminescence background increases and overshadows the Raman spectra. UV Raman, if carefully performed to avoid damage, allows us to get a spectrum of polymeric a-C:H and to correlate it with the film properties (Ferrari & Robertson 2000; Casiraghi *et al*. 2004*b*). Furthermore, figure 26 plots the comparison of the second-order spectral regions of a polymeric a-C:H and a polymeric a-C:D. This shows that the *ca.* 2920 cm^{-1} CH_x stretching modes can be detected in UV Raman, as confirmed by the downshift of this band to *ca.* 2100–2200 cm^{-1} upon deuterium substitution (Ferrari & Robertson 2000). Note as well that the peak intensity of the CD_x vibrations is roughly one-half of the intensity of the corresponding CH_x stretching modes, as is expected when considering the effect of H–D substitution on the Raman intensity.

Figure 19 shows that the intensity ratio of the sp CN peak to the G peak, $I(CN)/I(\mathrm{G})$, increases by almost one order of magnitude, moving from 514.5 to 244 nm excitation. Indeed, while it can be difficult to get a precise trend of

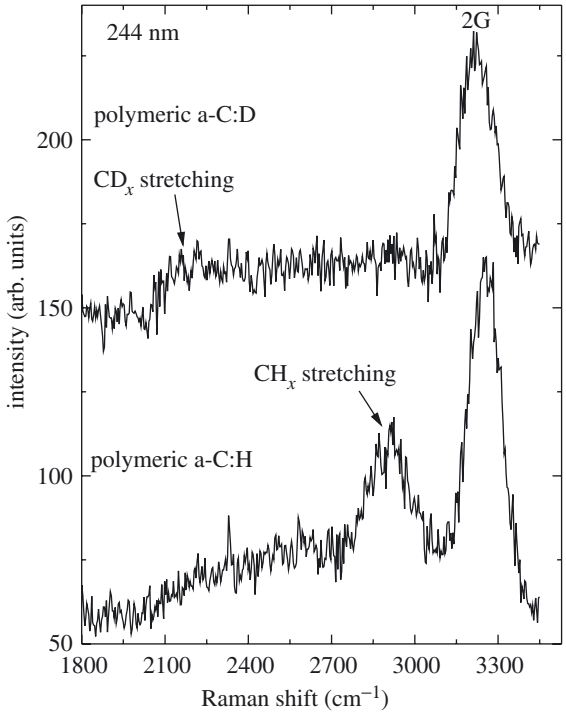

Figure 26. Comparison between the second-order region of the 244 nm Raman spectra of polymeric a-C:H and a-C:D samples. Note the downshift of the band at *ca.* 2920 cm^{-1} to *ca.* 2100–2200 cm^{-1} upon deuteration, and the *ca.* 50% reduction of its relative intensity, as is expected for C–H stretching vibrations compared with C–D ones.

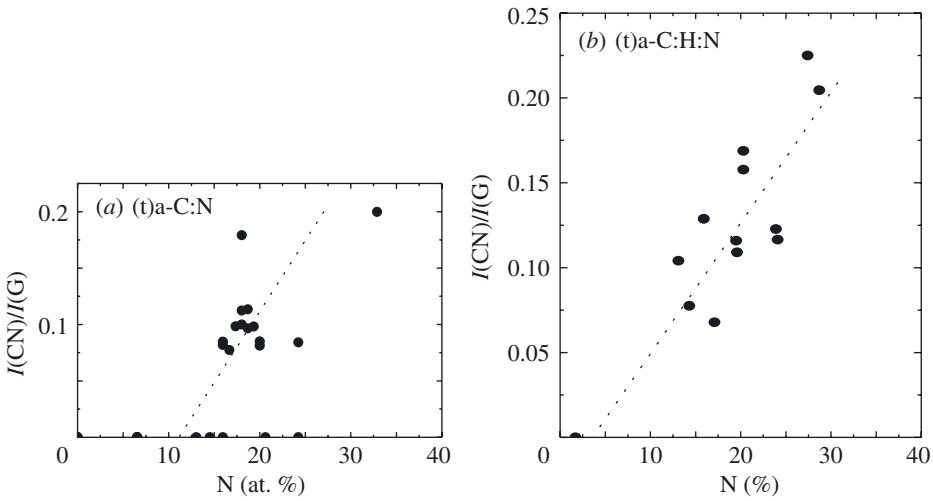

Figure 27. Variation of $I(CN)/I(\mathrm{G})$ as a function of N content for (*a*) (t)a-C:N samples and (*b*) (t)a-C:H:N samples.

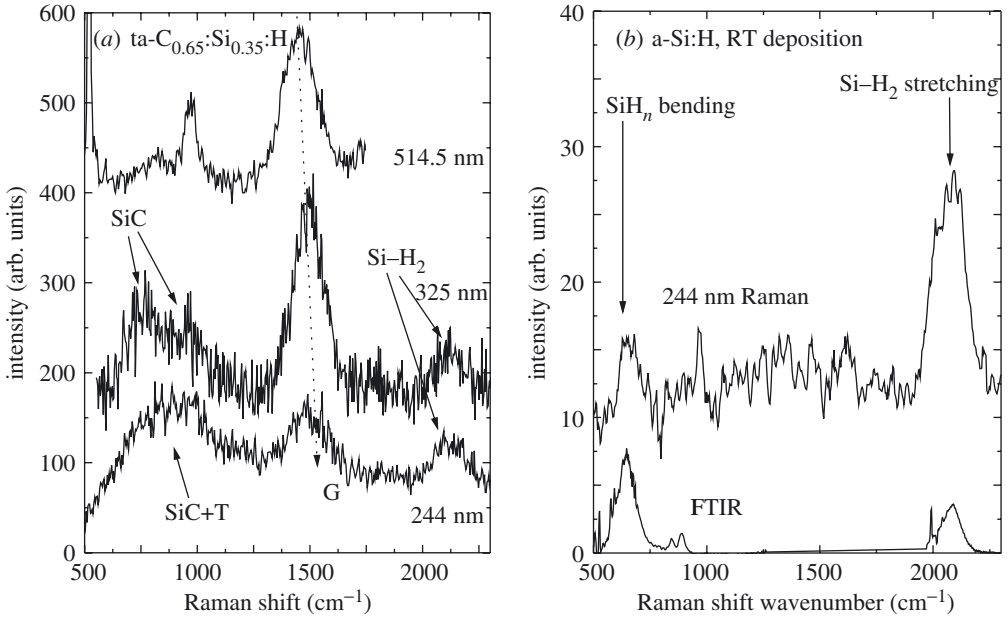

Figure 28. (*a*) Multi-wavelength Raman spectra of a ta-$C_{0.65}$:$Si_{0.35}$:H sample. For UV excitation the SiC modes and the Si–H_2 stretching are seen. (*b*) Comparison of 244 nm Raman and IR spectra of an a-Si:H sample deposited at room temperature, with 30 at. % H.

$I(CN)/I(\mathrm{G})$ for 514.5 excitation (Rodil *et al*. 2001), the use of UV Raman spectra allows us to get a linear correlation between $I(CN)/I(\mathrm{G})$ and the N content (figure 27). The enhancement of the sp^1 CN groups in UV excitation occurs because these groups have a π–π^* band gap of 5–6 eV. A similar trend is observed for all carbon nitrides (Ferrari *et al*. 2003). However, this trend is stronger and better defined for hydrogenated carbon nitride films (figure 27*b*). This shows that N is less likely to form sp^1 sites in ta-C:N than in the softer materials (Weich *et al*. 1997; Frauenheim *et al*. 1998).

Figure 28*a* plots the Raman spectra of an amorphous carbon silicon alloy with $\mathrm{Si}/(\mathrm{C}+\mathrm{Si}) = 0.35$ taken at different excitation energies. The UV Raman spectra show two extra features at *ca.* 760 and 960 cm^{-1}, corresponding to the peaks in the VDOS of SiC, as expected for an amorphous silicon carbide (Karch *et al*. 1994). These peaks are almost never detected in visible Raman spectra of a-SiC alloys, due to the small cross-section of Si-C vibration. Figure 28*b* compares the IR and the UV Raman spectra of a a-Si:H film deposited at room temperature. In this case, the band at *ca.* 2100 cm^{-1} is due to Si–H_2 stretching (Lucovsky *et al*. 1979; Racine *et al*. 2001), and it is also seen in UV Raman spectra of the (t)a-$C_{0.65}$:$Si_{0.35}$:H alloy in figure 28*a*. The band at *ca.* 650 cm^{-1} is due to SiH_n bending (Lucovsky *et al*. 1979; Racine *et al*. 2001).

7. Raman spectra of nanocrystalline diamond

The contribution of Prawer & Nemanich (2004) to this Theme Issue describes in detail the Raman spectrum of diamond and doped diamond. Here we consider the non-diamond phase in the Raman spectra of nanodiamond.

Figure 29 shows a Raman spectrum of a typical nanocrystalline diamond. In addition to a small diamond peak at 1332 cm^{-1}, the spectrum has four extra features at 1150, 1350, 1480 and 1550 cm^{-1}. The peaks at 1350 cm^{-1} and 1550 cm^{-1} are the D and G peaks of amorphous carbon. The peak at 1150 cm^{-1} has been attributed to nanocrystalline diamond (Nemanich *et al*. 1988; Shroder *et al*. 1990; Yarbrough & Messier 1990). Many researchers have since followed this assignment. However, we demonstrated by analysing the Raman spectra taken at different excitation energies that this peak and the companion peak at *ca*. 1480 cm^{-1} are a signature of trans-polyacetylene (Ferrari & Robertson 2001*a*) and have nothing to do with C–C sp^3 vibrations. We refer to these peaks as ν_1 and ν_3, respectively. In the following we review the evidence upon which we based our attribution and complement it with annealing and isotope-substitution data.

If the 1150 cm^{-1} peak arises from nanocrystalline or amorphous diamond, we may expect that it arises because the small grain size relaxes the $\boldsymbol{q} = \boldsymbol{0}$ Raman fundamental selection rule and allows phonon modes with $q \neq 0$ to contribute. This is ruled out for several reasons. First, the usual grain size of films which show this peak is too large to allow the activation of a zone boundary peak at *ca*. 1150 cm^{-1}. Phonon confinement allows the participation of phonons with wave vector $q \approx 2\pi/d$, where d is the grain size. Grains of 5–100 nm would still favour modes quite close to Γ, rather than modes nearer the zone boundary at L, where the VDOS maximum is (Pavone *et al*. 1993). Even if the grain sizes were truly 1 nm or less, the VDOS maximum is at 1260 cm^{-1}, not 1150 cm^{-1}, so a single peak at 1150 cm^{-1} would not be seen. The phonons in small grains could be softer than they are in bulk diamond. However, the Raman spectra of diamond nanocrystals from shock synthesis, with a fairly uniform distribution of grain sizes of 4–6 nm, were measured by Yoshikawa *et al*. (1993, 1995), Obraztsova *et al*. (1996) and Nistor *et al*. (1997). They saw only the main diamond peak broadened and downshifted by *ca*. 12–13 cm^{-1}, consistent with phonon confinement (Ager *et al*. 1991), confirming that bulk phonon dispersion curves are valid for nanometre-sized grains.

Figure 30 shows the Raman spectra taken at various laser excitation energies for the sample in figure 29. The ν_1 and ν_3 peaks disperse by 50–100 cm^{-1} with excitation energy. This is not possible for a density-of-states feature, which should remain fixed as the excitation energy varies. The intensity of the ν_1 and ν_3 peaks decreases compared with that of the 1332 cm^{-1} diamond peak, as the excitation energy is raised. If the two modes were both due to sp^3 sites, they would both increase in intensity as the excitation energy is raised. The 1150 cm^{-1} mode is, on the contrary, absent at 244 nm excitation. This is the opposite of what happens to the T peak in carbon films. The T peak is truly due to C–C sp^3 vibrations and appears only in the UV, as discussed in § 4 *c*, *d*.

The 1150 cm^{-1} mode always has a companion mode at *ca*. 1480 cm^{-1}. This is seen in figure 29, but it is sometimes obscured by the tail of the G peak of the disordered carbon phase at 1560 cm^{-1}. The spectra of figure 29 can be fitted with four Lorentzians, with all parameters free. The D and G peaks are then subtracted to give the residual intensity, shown in figure 31*a*. The calculated ν_1 and ν_3 dispersions for trans-polyacetylene are compared in figure 31*b* with the measured dispersions of the 1150 and 1450 cm^{-1} peaks. The measured modes closely follow the theoretical dispersions. The 1150 and 1450 cm^{-1} peaks are thus the ν_1 and ν_3 modes of trans-polyacetylene (explaining our terminology). A detailed discussion of the vibrations

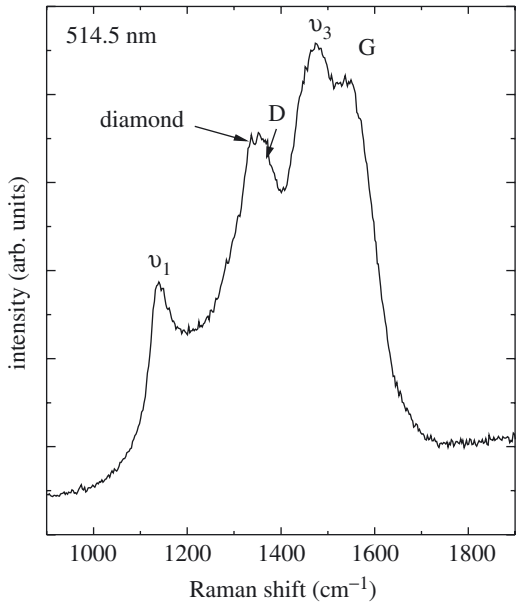

Figure 29. Visible Raman spectrum of a typical nanodiamond sample.

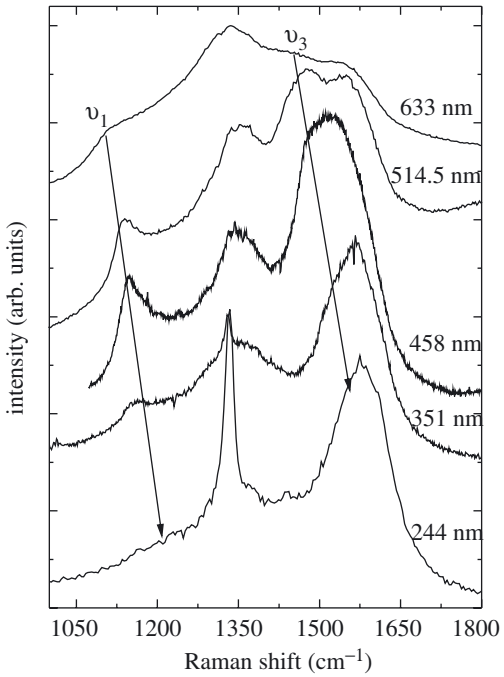

Figure 30. Multi-wavelength Raman spectra of the nanodiamond sample in figure 29.

and Raman spectra of trans-polyacetylene is found in the contribution of Castiglioni *et al*. (2004).

In a surface-enhanced Raman spectroscopy study of trans-polyacetylene in CVD diamond, a small peak at *ca*. 1240 cm^{-1} was also detected (López-Ríos *et al*. 1996).

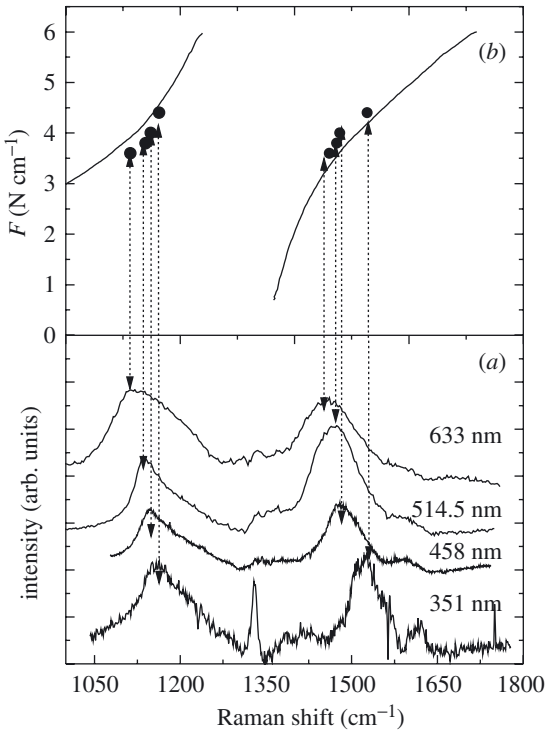

Figure 31. (*a*) Raman spectra of the nanodiamond in figure 29 after removal of the D and G peaks of the a-C phase. This leaves the diamond mode 1332 cm^{-1} (non-dispersive) and the dispersive v_1 and v_3 modes. (*b*) Comparison of the dispersion of the v_1 and v_3 modes with the theoretical dispersion of transpolyacetylene (see Castiglioni *et al*. 2004).

This peak is further evidence of trans-polyacetylene, as it normally has a third peak, ν_2, at this frequency, with smaller intensity than ν_1 and ν_3 and a very small dispersion with excitation energy (Ehrenfreund *et al*. 1987; Gussoni *et al*. 1991). Usually this third peak is not observed, due to its small intensity and the dominance of the D peak at that frequency.

The ν_1 and ν_3 modes of trans-polyacetylene are clearly connected to the presence of hydrogen. Indeed, a post-deposition annealing causes them to disappear (Obraztsova *et al*. 1996; Nistor *et al*. 1997; Pfeiffer *et al*. 2003; Ferrari *et al*. 2004) as shown in figure 32. The need for hydrogen also explains why these modes are not seen in nanocrystalline diamond prepared by shock synthesis (Yoshikawa *et al*. 1993, 1995; Obraztsova *et al*. 1996; Nistor *et al*. 1997).

A further direct proof of the presence of trans-polyacetylene in nanodiamond comes from H–D substitution. Ferrari *et al*. (2004) undertook an investigation of a variety of samples grown from deuterated and hydrogenated plasmas. A combination of CH_4/H_2, CD_4/H_2, CH_4/D_2 and CD_4/D_2 mixtures with an appropriate inert gas was used to independently grow an extensive set of samples in three different laboratories. A Raman investigation of these samples was performed with a variety of excitation wavelengths, from visible to UV. In the fully deuterated samples the Raman mode at *ca.* 1150 cm^{-1} disappears and is replaced by a new line at 860 cm^{-1} and the mode at *ca.* 1480 cm^{-1} downshifts to *ca.* 1450 cm^{-1} (figure 33). This isotopic shift again

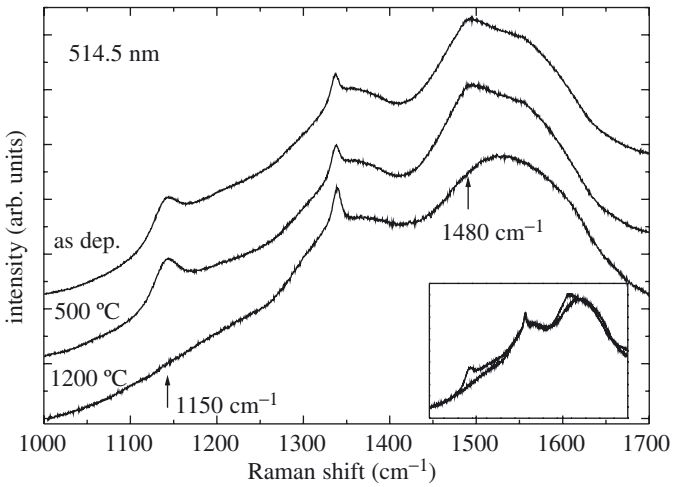

Figure 32. Comparison of the visible Raman spectra of nanodiamond annealed in vacuum after deposition. The v_1 and v_3 modes disappear, while the rest of the spectrum is substantially unchanged, as shown in the inset.

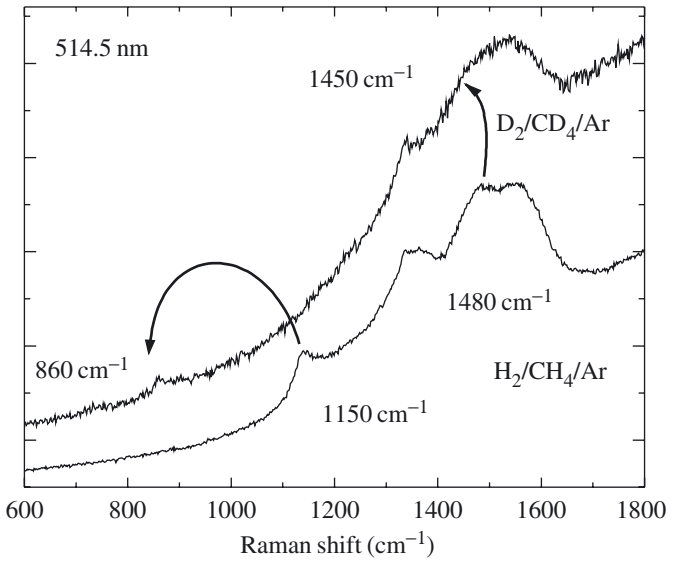

Figure 33. Comparison of the visible Raman spectra of a nanodiamond grown from deuterated precursors with the spectrum of a nanodiamond grown from hydrogenated precursors. Upon deuteration, the v_1 and v_3 modes move to the corresponding shifts of deuterated transpolyacetylene.

demonstrates that these modes are not due to C–C sp^3 vibrations. Furthermore, the isotopic shift matches the shift expected for deuterated trans-polyacetylene (Harada *et al*. 1980). The peaks' dispersion with excitation energy matches the dispersion of deuterated trans-polyacetylene (Harada *et al*. 1980). Post-deposition annealing of deuterated nanodiamond again causes the modes of deuterated trans-polyacetylene to disappear.

As discussed in § 4, UV Raman also allows the detection of C–H and C–D stretching vibrations. The nature of the amorphous carbon phase co-deposited with nanodiamond can be studied with multi-wavelength Raman spectroscopy. The comparative analysis of the Raman spectra for the different isotopic mixtures allows us to monitor the role of CH_4 and H_2 in the nanodiamond films growth (Ferrari *et al*. 2004).

8. Conclusions

We reviewed the interpretation of the Raman spectra of amorphous, nanostructured, diamond-like carbon, and nanodiamond. Raman spectroscopy is an extremely useful tool to determine the structure and composition of carbon films with and without nitrogen.

The authors thank the many people that allowed the work reviewed in this paper to be performed. All the data presented here on sp^3 content, H content, N content, gap, etc., were directly measured for every sample. We thank S. E. Rodil, C. Casiraghi, C. Castiglioni, M. Tommasini, F. Mauri, S. Piscanec, R. Ohr, M. VonGradowsky, B. Racine, H. Hilgers, D. Schneider, M. G. Beghi, D. Batchelder, M. Stutzmann, M. Kuball, D. Richards, D. Roy, B. Clyne, C. E. Bottani, R. Pfeiffer, H. Kuzmany, J. A. Zapien, Y. Lifshitz, N. Salk, B. Günther, Y. Wu, W. J. Zhang, I. Bello, J. Achard, F. Bénédic, A. Gicquel. A.C.F. acknowledges financial support from The Royal Society.

References

Ager III, J. W., Veirs, D. K. & Rosenblatt, G. M. 1991 *Phys. Rev.* B **43**, 6491.

Angus, J. C. & Hayman, C. C. 1998 *Science* **241**, 913.

Badzian, A., Badzian, T., Roy, R. & Drawl, W. 1999 *Thin Solid Films* **354**, 148.

Casiraghi, C., Ferrari, A. C., Robertson, J., Ohr, R., Gradowski, M., Schneider, D. & Hilgers, H. 2004*a* *Diamond Relat. Mater.* **13**, 1480.

Casiraghi, C., Ferrari, A. C., Grambole, D., Piazza, F. & Robertson, J. 2004*b* (Submitted.)

Castiglioni, C., Negri, F., Rigolio, M. & Zerbi, G. 2001 *J. Chem. Phys.* **115**, 3769.

Castiglioni, C., Di Donato, E., Tommasini, M., Negri, F. & Zerbi, G. 2003 *Synth. Metals* **139**, 885.

Castiglioni, C., Tommasini, M. & Zerbi, G. 2004 *Phil. Trans. R. Soc. Lond.* A **362**, 2425–2459.

Chowdhury, A. K. M. S., Cameron, D. C. & Hashimi, M. S. J. 1998 *Thin Solid Films* **332**, 62.

Conway, N. M. J., Ferrari, A. C., Flewitt, A. J., Robertson, J., Milne, W. I., Tagliaferro, A. & Beyer, W. 2000 *Diamond Relat. Mater.* **9**, 765.

Cutiongco, E. C., Li, D., Chung, Y. W. & Bhatia, C. S. 1996 *J. Tribol.* **118**, 543.

Dollish, F. R., Fateley, W. G. & Bentley, F. F. 1974 *Characteristic Raman frequencies of organic molecules*. Wiley.

Drabold, D. A., Fedders, P. A. & Strumm, P. 1994 *Phys. Rev.* B **49**, 16415.

Dubay, O. & Kresse, G. 2003 *Phys. Rev.* B **67**, 035401.

Ehrenfreund, E., Vardeny, Z., Brafman, O. & Horovitz, B. 1987 *Phys. Rev.* B **36**, 1535.

Ferrari, A. C. 2004 *Surf. Coat. Technol.* **180**, 190.

Ferrari, A. C. & Robertson, J. 2000 *Phys. Rev.* B **61**, 14095.

Ferrari, A. C. & Robertson, J. 2001*a* *Phys. Rev.* B **63**, R121405.

Ferrari, A. C. & Robertson, J. 2001*b* *Phys. Rev.* B **64**, 075414.

Ferrari, A. C., Rodil, S. E. & Robertson, J. 2003 *Phys. Rev.* B **67**, 155306.

Ferrari, A. C. (and 16 others) 2004 (Submitted.)

Frauenheim, T., Jungnickel, G., Sitch, P., Kaukonen, M., Weich, F., Widany, J. & Porezag, D. 1998 *Diamond Relat. Mater.* **7**, 348.

Fung, M. K., Chan, W. C., Gao, Z. Q., Bello, I. & Lee, S. T. 1999 *Diamond Relat. Mater.* **8**, 472.

Gammon, W. J., Malyarenko, D. I., Kraft, O., Hoatson, G. L., Reilly, A. C. & Holloway, B. C. 2002 *Phys. Rev.* B **66**, 153402.

Gammon, W. J., Hoatson, G. L., Holloway, B. C., Vold, R. L. & Reilly, A. C. 2003 *Phys. Rev.* B **68**, 195401.

Gangopadhyay, A. K., Willermet, P. A., Tamor, M. A. & Vassel, W. C. 1997 *Tribol. Int.* **30**, 9.

Gilkes, K. W. K., Sands, H. S., Batchelder, D. N., Robertson, J. & Milne, W. I. 1997 *Appl. Phys. Lett.* **70**, 1980.

Gilkes, K. W. R., Prawer, S., Nugent, K. W., Robertson, J., Sands, H. S., Lifshitz, Y. & Shi, X. 2000 *J. Appl. Phys.* **87**, 7283.

Grill, A. 2001 *Diamond Relat. Mater.* **10**, 234.

Gruen, D. M. 1999 *A. Rev. Mater. Sci.* **29**, 211.

Gruneis, A., Saito, R., Kimura, T., Cancado, L. G., Pimenta, M. A., Jorio, A., Souza Filho, A. G., Dresselhaus, G. & Dresselhaus, M. S. 2002 *Phys. Rev.* B **65**, 155405.

Gussoni, M., Castiglioni, C. & Zerbi, G. 1991 In *Spectroscopy of advanced materials* (ed. R. J. Clark & R. E. Hester), p. 251. Wiley.

Harada, I. *et al*. 1980 *J. Chem. Phys.* **73**, 4746.

Hellgren, N., Johansson, M. P., Broitman, E., Hultman, L. & Sundgren, J. E. 1999 *Phys. Rev.* B **59**, 5162.

Ilie, A., Ferrari, A. C., Yagi, T. & Robertson, J. 2000 *Appl. Phys. Lett.* **76**, 2627.

Jimenez, I., Gago, R., Albella, J. M., Caceres, D. & Vergara, I. 2000 *Phys. Rev.* B **62**, 4261.

Karch, K., Pavone, P., Windl, W., Shutt, O. & Strauch, D. 1994 *Phys. Rev.* B **50**, 17045.

Katkritzki, A. R. (ed.) 1963 *Physical methods in heterocycle chemistry*, vol. II. Academic.

Katkritzki, A. R. (ed.) 1971 *Physical methods in heterocycle chemistry*, vol. IV. Academic.

Kohler, T., Frauenheim, T. & Jungnickel, G. 1995 *Phys. Rev.* B **52**, 11837.

Kohn, W. 1959 *Phys. Rev. Lett.* **2**, 393.

Koidl, P., Wagner, C., Dischler, B., Wagner, J. & Ramsteiner, M. 1990 *Mater. Sci. Forum* **52**, 41.

Kresse, G., Furthmuller J. & Hafner, J. 1995 *Europhys. Lett.* **32**, 729.

Liu, A. Y. & Cohen, M. L. 1989 *Science* **245**, 841.

López-Ríos, T., Sandre', E., Leclerq, S. & Sauvain, E. 1996 *Phys. Rev. Lett.* **76**, 4935.

Lopinski, G. P., Merkulov, V. I. & Lannin, J. S. 1996 *Appl. Phys. Lett.* **69**, 3348.

Lucovsky, G., Nemanich, R. J. & Knights, J. 1979 *Phys. Rev.* B **19**, 2064.

Mapelli, C., Castiglioni, C., Zerbi, G. & Mullen, K. 1999 *Phys. Rev.* B **60**, 12710.

Marchon, B., Gui, J., Grannen, K., Rauch, G. C., Ager, J. W., Silva, S. R. P. & Robertson, J. 1997 *IEEE Trans. Magn.* **33**, 3148.

Matsuda, A. & Tanaka, K. 1987 *J. Non-cryst. Solids* **97**, 1367.

Matsumoto, S., Xie, E. Q. & Izumi, F. 1999 *Diamond Relat. Mater.* **8**, 1175.

Matthews, M. J., Pimenta, M. A., Dresselhaus, G., Dresselhaus, M. S. & Endo, M. 1999 *Phys. Rev.* B **59**, 6585.

Maultzsch, J., Reich, S., Thomsen, C., Requardt, H. & Ordejon, P. 2004 *Phys. Rev. Lett.* **92**, 075501.

Mauri, F. & Del Corso, A. 1999 *Appl. Phys. Lett.* **75**, 644.

Merkulov, V. I., Lannin, J. S., Munro, C. H., Asher, S. A., Veerasamy, V. S. & Milne, W. I. 1997 *Phys. Rev. Lett.* **78**, 4869.

Milani, P. & Iannotta, S. 1999 *Cluster beam synthesis of nanostructured materials*. Springer.

Milani, P., Ferretti, M., Piseri, P., Bottani, C. E., Ferrari, A. C., LiBassi, A., Guizzetti, G. & Patrini, M. 1997 *J. Appl. Phys.* **82**, 5793.

Morrison, N. A., Rodil, S. E., Ferrari, A. C., Robertson, J. & Milne, W. I. 1999 *Thin Solid Films* **337**, 71.

Muhl, S. & Mendez, J. M. 1999 *Diamond Relat. Mater.* **8**, 1809.

Nemanich, R. J., Glass, J. T., Lucovsky, G. & Shroder, R. E. 1988 *J. Vac. Sci. Technol.* A **6**, 1783.

Nistor, L. C., Van Landuyt, J., Ralchenko, V. G., Obratzova, E. D. & Smolin, A. A. 1997 *Diamond Relat. Mater.* **6**, 159.

Obraztsova, E. D., Kuznetsov, V. L., Loubnin, E. N., Pimenov, S. M. & Pereverzev, V. G. 1996 In *Nanoparticles in solids and solutions* (ed. J. H. Fendler & I. Dekany). Deventer: Kluwer.

Oguri, K. & Arai, T. 1992 *Thin Solid Films* **208**, 158.

Pavone, P., Karch, K., Shutt, O., Windl, W., Strauch, D., Giannozzi, P. & Baroni, S. 1993 *Phys. Rev.* B **48**, 3164.

Pavone, P., Bauer, R., Karch, K., Schutt, O., Vent, S., Windl, W., Strauch, D., Baroni, S. & de Gironcoli, S. 1996 *Physica* B **219–220**, 439.

Pfeiffer, R., Kuzmany, H., Knoll, P., Bokova, S., Salk, N. & Gunther, B. 2003 *Diamond Relat. Mater.* **12**, 268.

Piscanec, S., Lazzeri, M., Mauri, F., Ferrari, A. C. & Robertson, J. 2004*a* *Phys. Rev. Lett.* (In the press.)

Piscanec, S., Ferrari, A. C., Lazzeri, M., Mauri, F., Reich, S. & Robertson, J. 2004*b* The limit of ballistic transport in metallic nanotubes. (In preparation.)

Piscanec, S., Ferrari, A. C., Lazzeri, M., Mauri, F. & Robertson, J. 2004*c* *Diamond Relat. Mater.* (In the press.)

Pócsik, I., Hundhausen, M., Koos, M. & Ley, L. 1998 *J. Non-cryst. Solids* **227–230**, 1083.

Prawer, S. & Nemanich, R. J. 2004 *Phil. Trans. R. Soc. Lond.* A **362**, 2537–2565.

Profeta, M. & Mauri, F. 2001 *Phys. Rev.* B **63**, 245415.

Racine, B., Ferrari, A. C., Morrison, N. A., Hutchings, I., Milne, W. I. & Robertson, J. 2001 *J. Appl. Phys.* **90**, 5002.

Ravagnan, L., Siviero, F., Lenardi, C., Piseri, P., Barborini, E., Milani, P., Casari, C. S., Li-Bassi, A. & Bottani, C. E. 2002 *Phys. Rev. Lett.* **89**, 285506.

Reich, S. & Thomsen, C. 2004 *Phil. Trans. R. Soc. Lond.* A **362**, 2271–2288.

Ristein, J., Stief, R. T., Ley, L. & Beyer, W. 1998 *J. Appl. Phys.* **84**, 3836.

Robertson, J. 2002 *Mater. Sci. Engng* **R37**, 129.

Rodil, S. E., Ferrari, A. C., Robertson, J. & Milne, W. I. 2001 *J. Appl. Phys.* **89**, 5425.

Saito, R., Jorio, A., Souza Filho, A. G., Dresselhaus, G., Dresselhaus, M. S. & Pimenta, M. A. 2002 *Phys. Rev. Lett.* **88**, 027401.

Salis, S. R., Gardiner, D. J., Bowden, M., Savage, J. & Rodway, D. 1996 *Diamond Relat. Mater.* **5**, 589.

Shroder, R. E., Nemanich, R. J. & Glass, J. T. 1990 *Phys. Rev.* B **41**, 3738.

Tamor, M. A. & Vassel, W. C. 1994 *J. Appl. Phys.* **76**, 3823.

Thomsen, C. & Reich, S. 2000 *Phys. Rev. Lett.* **85**, 5214.

Tuinstra, F. & Koening, J. L. 1970 *J. Chem. Phys.* **53**, 1126.

Voevodin, A. A., Schneider, J. M., Rebholz, C. & Matthews, A. 1996 *Tribol. Int.* **29**, 559.

Wada, N., Gaczi, P. J. & Solin, A. 1980 *J. Non-cryst. Solids* **35–36**, 543.

Weich, F., Widany, J. & Frauenheim, T. 1997 *Phys. Rev. Lett.* **78**, 3326.

Wirtz, L. & Rubio, A. 2004 *Solid State Commun.* **131**, 141.

Wixom, M. R. 1990 *J. Am. Ceram. Soc.* **73**, 1973.

Yap, Y. K., Kida, S., Aoyama, T., Mori, Y. & Sasaki, T. 1998 *Appl. Phys. Lett.* **73**, 915.

Yarbrough, W. A. & Messier, R. 1990 *Science* **247**, 688.

Yoshikawa, M., Mori, Y., Meagawa, M., Katagiri, G., Ishida, H. & Ishitani, A. 1993 *Appl. Phys. Lett.* **62**, 3114.

Yoshikawa, M., Mori, Y., Oabata, H., Maegawa, M., Katagiri, G., Ishsida, H. & Ishsitani, A. 1995 *Appl. Phys. Lett.* **67**, 694.